ELSEVIER

Contents lists available at ScienceDirect

# Ocean Engineering

journal homepage: www.elsevier.com/locate/oceaneng



# Research paper

# A multi-resolution MPS-PD coupling method for three-dimensional fluid-structure interaction involving fracture

Fengze Xie <sup>a</sup>, Jian Zhang <sup>b</sup>, Yifan Li <sup>a</sup>, Decheng Wan <sup>a,\*</sup>, Moustafa Abdel-Maksoud <sup>c</sup>

- a Computational Marine Hydrodynamics Lab (CMHL), School of Naval Architecture, Ocean and Civil Engineering, Shanghai Jiao Tong University, Shanghai, China
- <sup>b</sup> Ningbo Pilot Station, Ningbo Dagang Pilotage Co., Ltd., Ningbo, China
- c Institute for Fluid Dynamics and Ship Theory (M8), Hamburg University of Technology (TUHH), Hamburg, Germany

#### ARTICLE INFO

#### Keywords:

Moving particle semi-implicit method Peridynamics Fluid-structure interaction Multi-resolution Three dimensional simulations

#### ABSTRACT

In this paper, an in-house solver MPSPD-SJTU is developed to address 3D Fluid-Structure Interaction (FSI) problems with fracture. The Moving Particle Semi-implicit (MPS) method is utilized to simulate the violent freesurface flows while the PeriDynamics (PD) method is employed to model the structures with large deformations and fractures. Besides, a Kernel Function Based Interpolation Technique (KFBI) is incorporated into the coupling method to handle the MPS particles and PD particles with different resolutions. Firstly, the MPS solver is utilized to simulate dam break flow impacting a fixed obstacle, serving to evaluate its accuracy and reliability. Subsequently, the PD-based structural solver is validated by simulating an oscillating cantilever plate, a clamped-clamped elastic beam under uniformly distributed load, the Kalthoff-Winkler impact test, and three-point bending of an ice beam. Next, the MPS-PD model is validated via some benchmark tests, such as flood discharge with an elastic plate, hydrostatic water column on an elastic plate, dam-break flow with a hanging elastic plate, as well as dam-break flow with an elastic obstacle. The numerical results obtained in this study exhibit good agreement with experimental data as well as those from other numerical methods. Finally, the coupling model is applied to investigate the dam-break flow impacting a hanging elastic plate with a prefabricated crack.

#### 1. Introduction

Fluid-structure interaction phenomena are quite common in the field of ocean engineering. For instance, waves slamming on offshore structures (Fimreite et al., 2025; Zhao et al., 2024; Zhuang et al., 2023), liquid sloshing in transport vessels (Huang et al., 2023, 2024a; Xie et al., 2020), and the impact of tsunamis on nearshore structures (Iwamoto et al., 2019) are typical examples. The hydrodynamic loads in the ocean typically exhibit characteristics such as strong nonlinearity, dynamic behavior, and randomness, which may cause significant deformation and even fracture of structures. Therefore, it is essential to conduct research on these multi-physics interaction problems, so as to better understand and address these potential structural risks.

Experimental methods are reliable and provide irreplaceable validation for such problems. However, experiments incur high costs, require long lead times, and have limitations in simulating extreme scenarios. As effective supplements, numerical simulations reduce research expenses, enable flexible parameter adjustment and repeated testing, and safely explore extreme conditions, thus making them necessary.

According to the coupling strategies of FSI, numerical methods can be classified into the monolithic and partitioned approaches (Hwang et al., 2014). The monolithic approaches integrate the governing equations of the fluid and structural fields into a unified system of equations (Idelsohn et al., 2008). They simultaneously solve fluid variables (e.g., velocity, pressure) and structural variables (e.g., displacement, stress) through unified discretization schemes, directly reflecting the instantaneous FSI. Partitioned approaches treat the fluid field and solid field as independent systems, and then transfer information via interpolation/mapping algorithms at the fluid-structure interface (Li et al., 2015). The former exhibits superior stability and higher accuracy at the interface, while the latter possesses greater flexibility, higher computational efficiency, and ease of coupling different types of mature single-field solvers. Owing to these advantages, partitioned approaches are more suitable for solving engineering problems and have attracted extensive attention in the academic community in recent years.

E-mail address: dcwan@sjtu.edu.cn (D. Wan).

<sup>\*</sup> Corresponding author.

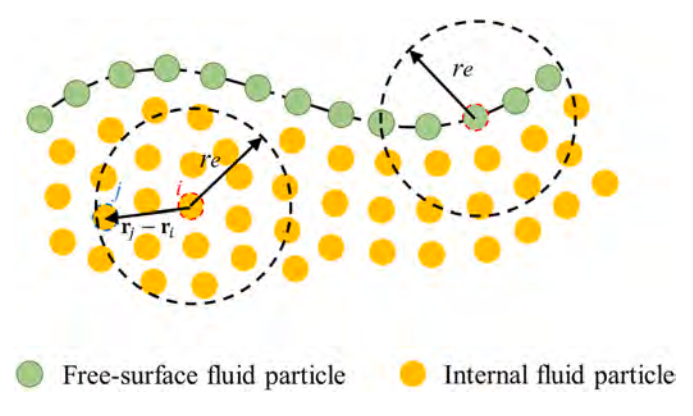


Fig. 1. Schematic of the free surface detection.

In partitioned approaches, different fields can be solved using their respective optimal numerical methods. Grid-based methods have relatively mature theories. They are characterized by high precision and strong stability. However, when facing intense flows (e.g., dam-break flows, wave slamming), meshes are easily distorted. As a consequence, computational accuracy is sharply reduced, and calculations may even be terminated. For this reason, frequent mesh reconstruction is required, which in turn increases complexity and computational costs. Particle-based methods, by contrast, are naturally suited to handling problems such as large deformations of free surfaces and moving boundaries (Xie et al., 2022). Although particle-based methods suffer from inherent issues such as low accuracy and poor stability in certain scenarios, many enhancement techniques have been proposed to improve their performance. For instance, the gradient model of momentum conservation (Tanaka and Masunaga, 2010) and the Particle Shifting Technique (PST)

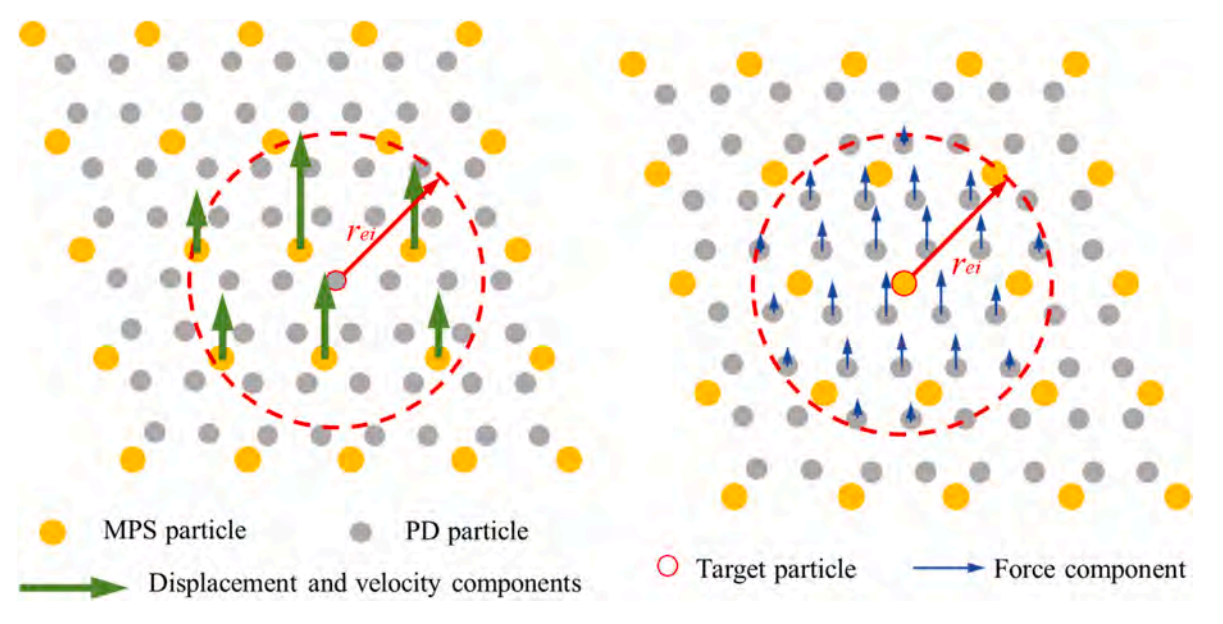


Fig. 2. Schematic of the KFBI technique.

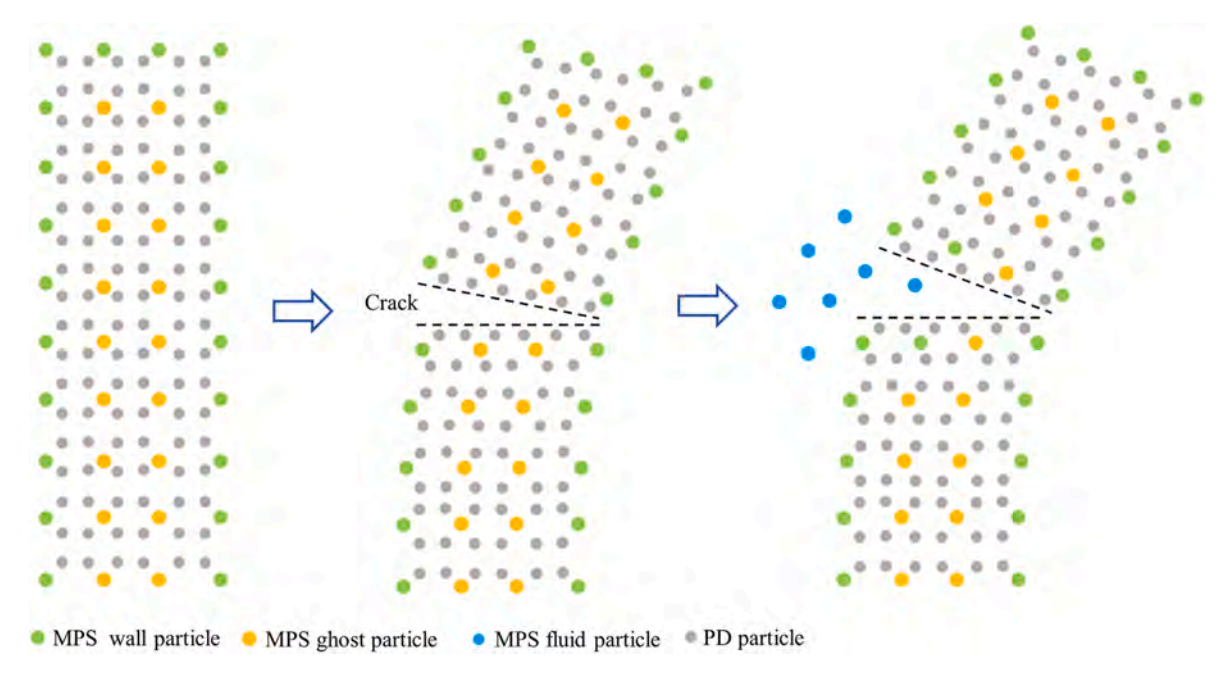


Fig. 3. Schematic of particle processing near the fracture surface.

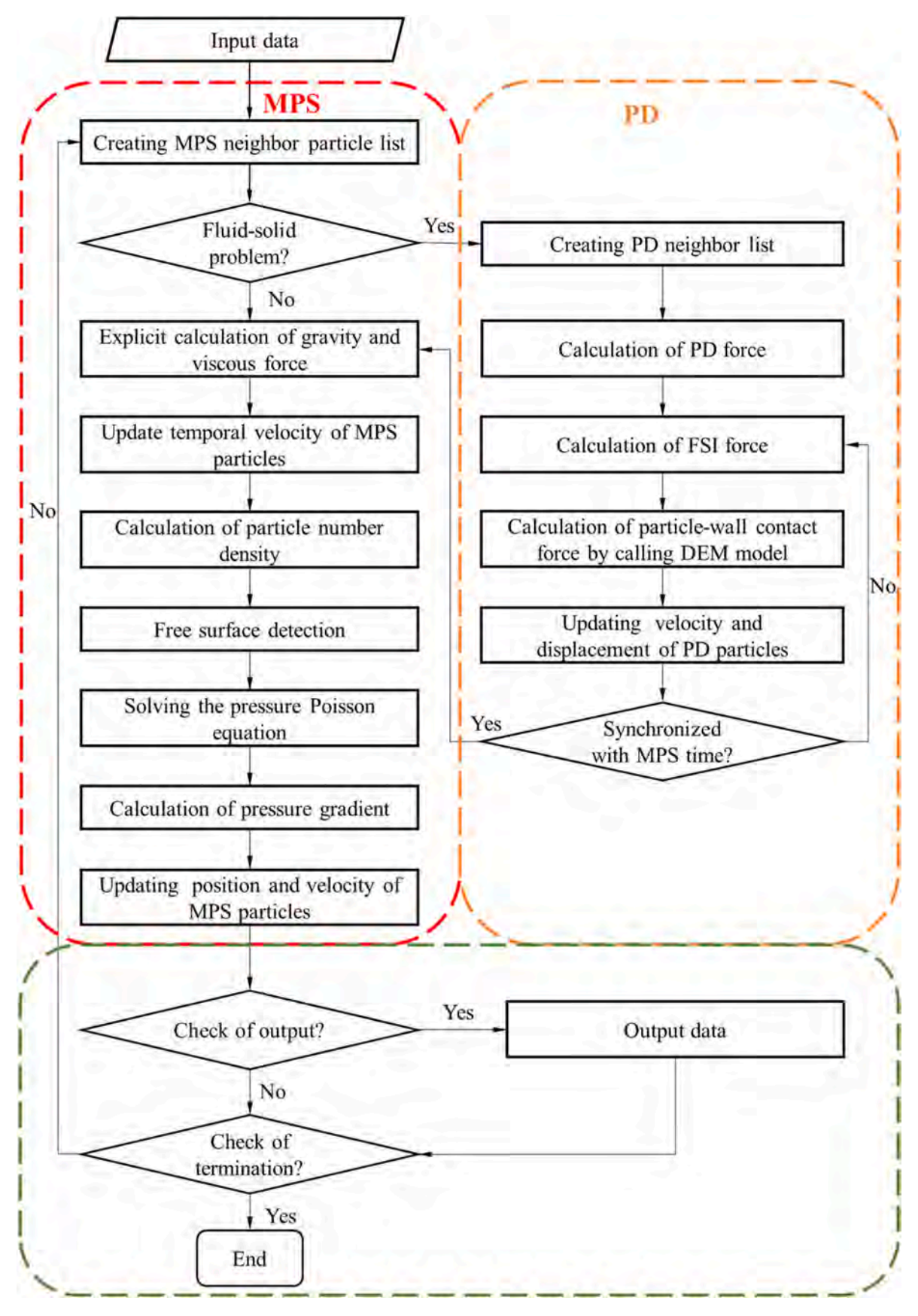


Fig. 4. Flowchart of the MPS-PD solver.

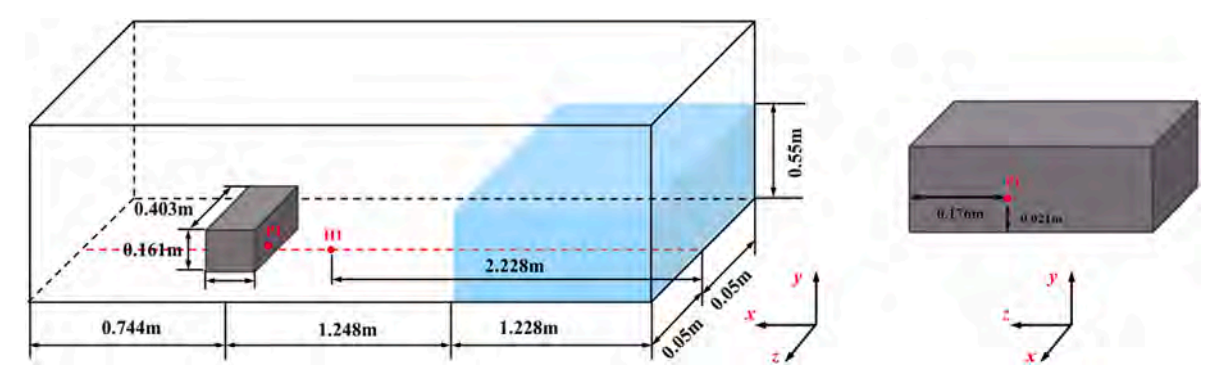
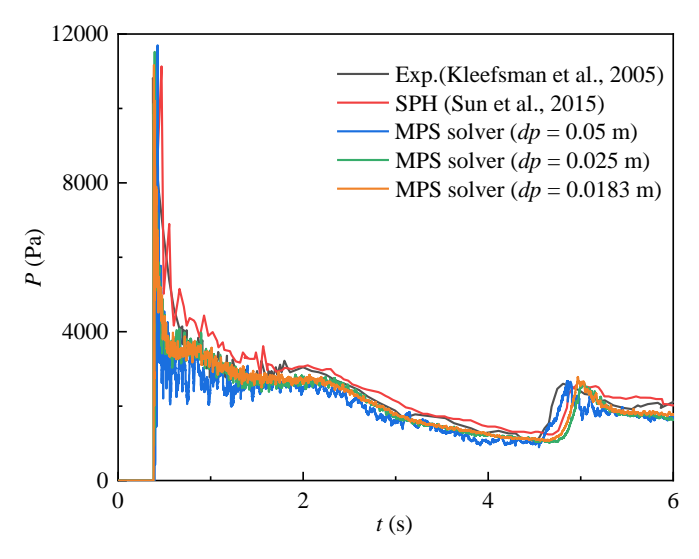


Fig. 5. Schematic of the numerical model - dam break flow impacting a fixed square obstacle.

**Table 1**Parameters in the simulation - dam-break flow impacting a fixed square obstacle.

MPS parameters	Values
Density (kg/ m³)	1000
Initial particle spacing (m)	0.0183, 0.025, 0.05
Viscosity (Pa· s)	$8.9\times10^{-5}$
Time step (s)	$5.0 imes10^{-4}$



**Fig. 6.** Comparison of pressure time histories at P1 among the results obtained by experiment (Kleefsman et al., 2005), SPH (Sun et al., 2015), and MPS with different resolutions - dam-break flow impacting a fixed square obstacle.

(Duan et al., 2018; Gao and Fu, 2023; Gotoh et al., 2024; Khayyer et al., 2023; Zhan et al., 2025a) have been proposed to prevent particles from aggregating. The mixed gradient model (Huang et al., 2022; Sun et al., 2018, 2019), also known as Tensile Instability Control (TIC), has been developed for simulating high Reynolds number flows involving negative pressure. Additionally, high-order schemes (Khayyer and Gotoh, 2011, 2012; Liu et al., 2019, 2025; Wang et al., 2023) have also been proposed to improve the accuracy of the model.

The Finite Element Method (FEM) is relatively mature and is often used to verify the accuracy of other structural analysis methods, which has been coupled with two widely used particle-based methods: the Smoothing Particle Hydrodynamics (SPH) and Moving Particle Semi-implicit (MPS). These coupling methods have been employed to investigate complicated FSI problems, such as ship hull water entry (Chen et al., 2025), wave-structure interaction (Ma et al., 2020; Zhang et al.,

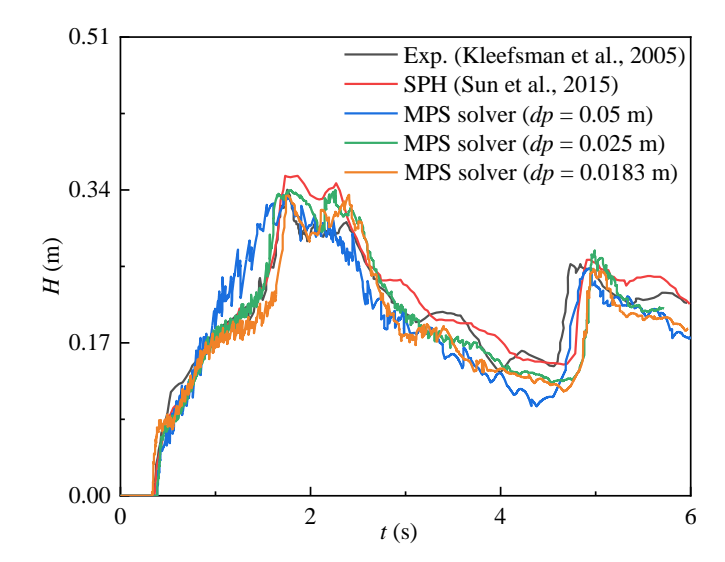


**Fig. 7.** Comparison of wave height time histories at H1 among the results obtained by experiment (Kleefsman et al., 2005), SPH (Sun et al., 2015), and MPS with different resolutions - dam-break flow impacting a fixed square obstacle.

2022b), sloshing flow-structure interaction (Zhang and Wan, 2018), etc. However, it is difficult for FEM to handle crack-tip singularities and accurately predict crack propagation paths.

Compared with the FEM, meshfree methods such as SPH and MPS do not rely on fixed mesh elements when handling large deformation problems. This fundamentally avoids the risk of mesh distortion and the need for remeshing, ensuring the stability and efficiency of the computation process. Both elastic structures and flow fields can also be modelled with SPH or MPS (Gotoh et al., 2021, 2025; Khayyer et al., 2022a; Zhan et al., 2025b). In order to improve the accuracy of the particle-based structural model, high-order schemes for the discretization of the deformation gradient tensor have been developed (Khayyer et al., 2024; Shimizu et al., 2022). Besides, the Riemann stabilization schemes (Khayyer et al., 2024; Shimizu et al., 2022) and hourglass control schemes (Wu et al., 2024; Zhan et al., 2025c; Zhang et al., 2025) have been introduced to the particle-based structural model to enhance the stability of the FSI solver. Models based on SPH or MPS have also been successfully extended to simulating problems such as the deformation of composite structures (Khayyer et al., 2021b, 2022b) and structural fracture, even though their ability to capture fracture details remains limited (Ren and Park, 2023; Singh et al., 2025). Ordinary SPH or MPS methods are essentially rooted in continuum mechanics, and their assumptions of continuity, reliance on partial differential equations (PDEs), and logic of local action conflict with the intrinsic features of fracture — discontinuity, singularity, and non-locality.

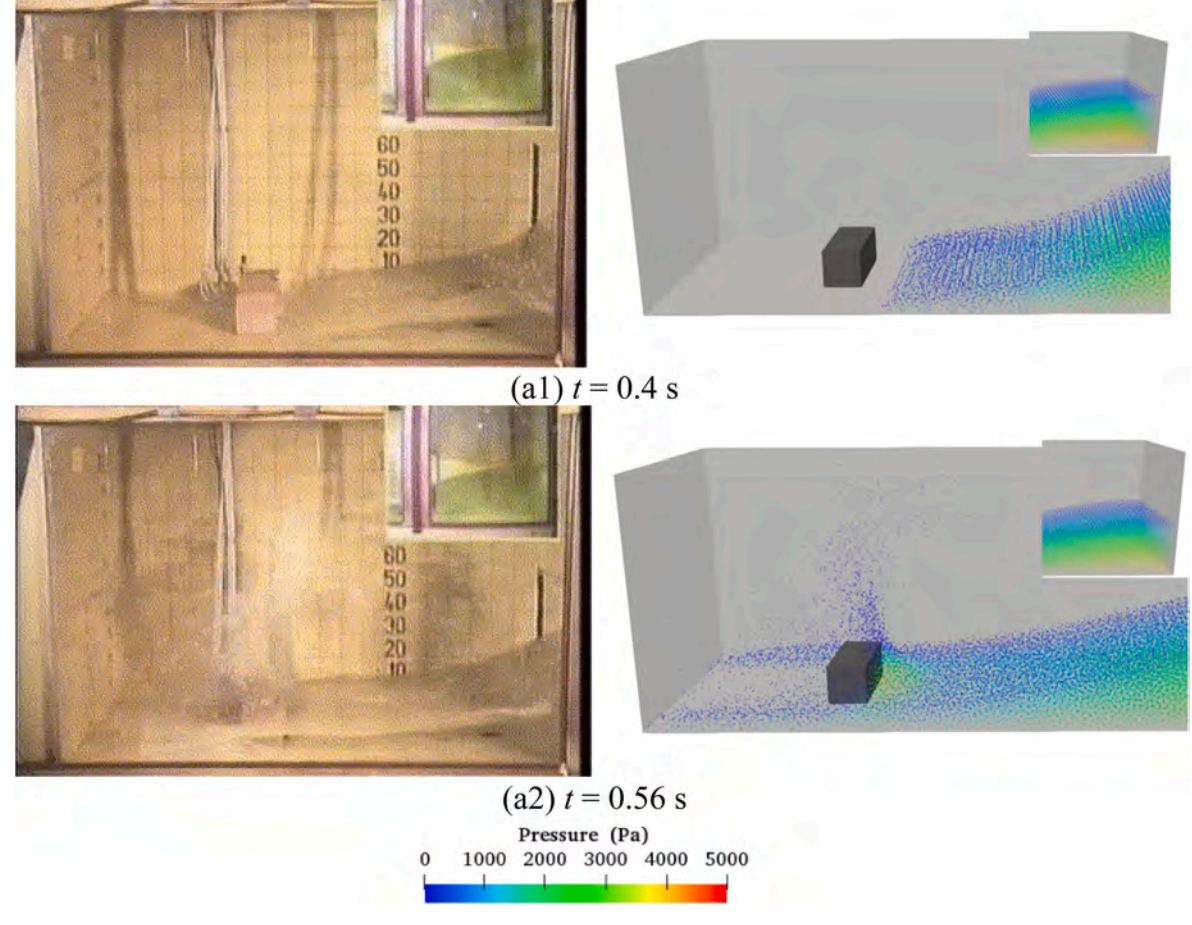
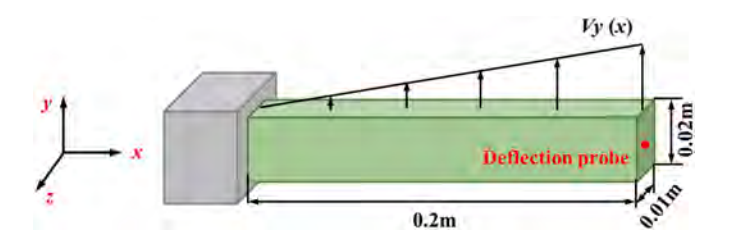


Fig. 8. Comparison of the dam-break flow morphologies between experimental snapshots (Kleefsman et al., 2005) and numerical results obtained by the MPS -dam-break flow impacting a fixed square obstacle.



 $\begin{tabular}{ll} {\bf Fig.~9.~Schematic~of~the~numerical~model~-~dynamic~response~of~an~oscillating~cantilever~beam.} \end{tabular}$ 

 $\begin{tabular}{ll} \textbf{Table 2} \\ \textbf{Parameters in the simulation - dynamic response of an oscillating cantilever} \\ \textbf{beam.} \\ \end{tabular}$ 

Values
1000
$2 \times 10^{-3}, 1 \times 10^{-3}, 6.67 \times 10^{-4}$
2.0
0.4
$5.0  imes 10^{-6}$

In recent years, a novel method—PeriDynamics (PD)—has been proposed by Silling (2000). Notably, this method employs integral equations to eliminate fracture singularities, achieves natural fracture through material point bonds, adapts to damage via non-locality, and enables efficient computation via a meshless framework. Its inherent

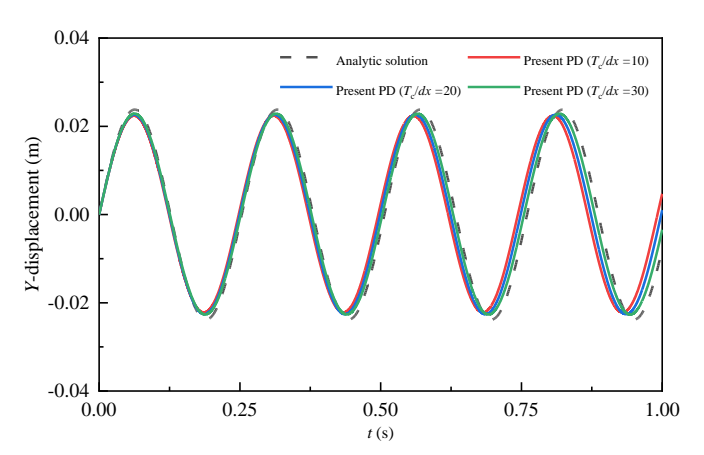


**Fig. 10.** Comparison of vertical displacement time histories between the analytic solution and PD results with different resolutions - dynamic response of an oscillating cantilever beam.

alignment with the nature of fracture endows it with unique advantages. Scholars have adopted the Immersed Boundary Method (IBM) to achieve the coupling of PD and grid-based methods (Dalla Barba et al., 2022; Yang et al., 2022). In contrast, PD and other particle-based methods possess an intrinsic compatibility advantage. PD has also been coupled with SPH for the simulation of violent FSI problems with large deformation of the free surface. Huang et al. (2024b) proposed a coupled SPH-PD model and applied it to simulate dam failure induced by

Fig. 11. The stress distribution of the cantilever beam at t = 0.57s - dynamic response of an oscillating cantilever beam.

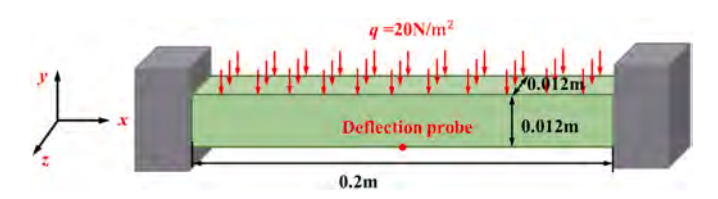


**Fig. 12.** Schematic of the numerical model - static deflection of a clamped-clamped elastic beam under uniform load.

 $\begin{tabular}{ll} \textbf{Table 3} \\ \textbf{Parameters in the simulation - static deflection of a clamped-clamped elastic beam under uniform load.} \\ \end{tabular}$ 

PD parameters	Values
Density (kg/ m³)	1000
Initial particle spacing (m)	$1 \times 10^{-3}, 8 \times 10^{-4}, 6.67 \times 10^{-4}$
Young's modulus (Pa)	$2.4 \times 10^{7}$
Poisson's ratio	0.25
Time step(s)	$5.0  imes 10^{-6}$

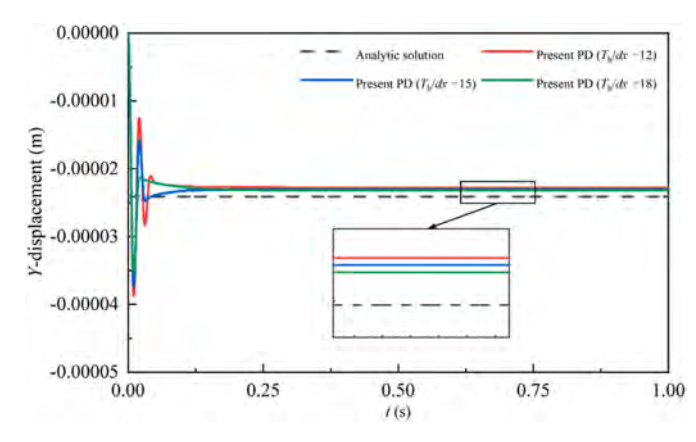


**Fig. 13.** Comparison of vertical displacement time histories between the analytic solution and PD results with different resolutions - static deflection of a clamped-clamped elastic beam under uniform load.

underwater explosions (Huang et al., 2025b) and soil fragmentation induced by buried explosions (Huang et al., 2025a). Yao and Huang (2022) also developed a SPH-PD model, which is employed to study water-jetting-induced rock fragmentation phenomena. A multi-resolution technique has also been introduced to this SPH-PD model (Yao and Huang, 2022). Liang et al. (2025b) established a 3D ice tank based on the SPH-PD model. SPH-PD models are also utilized to

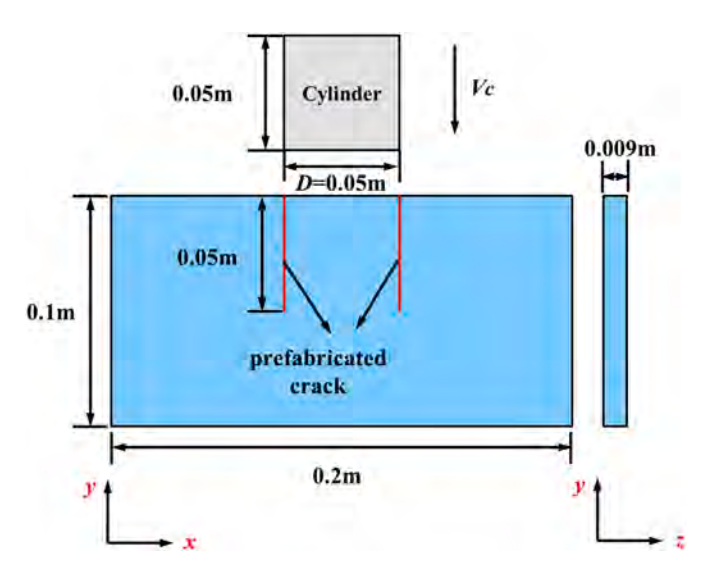


Fig. 15. Schematic of the numerical model - Kalthoff-Winkler impact test.

**Table 4**Parameters in the simulation - Kalthoff-Winkler impact test.

PD parameters	Values
Density (kg/m³)	8000
Initial particle spacing (m)	$1 imes10^{-3}$
Young's modulus (Pa)	$1.91\times10^{11}$
Poisson's ratio	0.25
Critical energy release rate (J/m <sup>2</sup> )	$6.91  imes 10^4$
Critical stretch $s_0$	0.01
Time step(s)	$1.0\times10^{-7}$

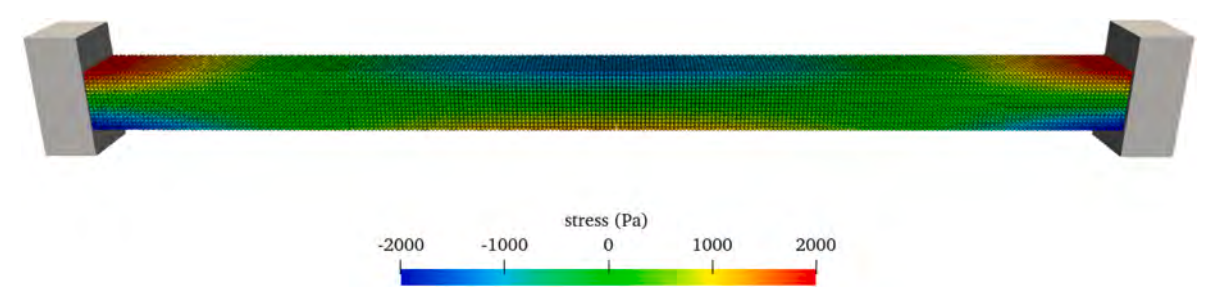
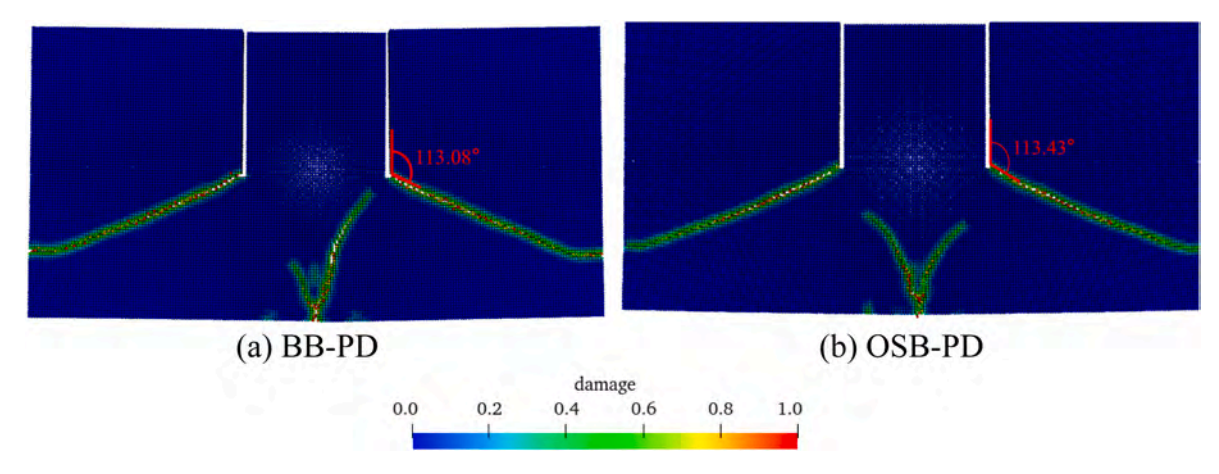


Fig. 14. The stress distribution of the beam after reaching steady state - static deflection of a clamped-clamped elastic beam under uniform load.



 $\textbf{Fig. 16.} \ \ \textbf{Crack path reproduced by BB-PD and OSB-PD - Kalthoff-Winkler impact test.}$ 

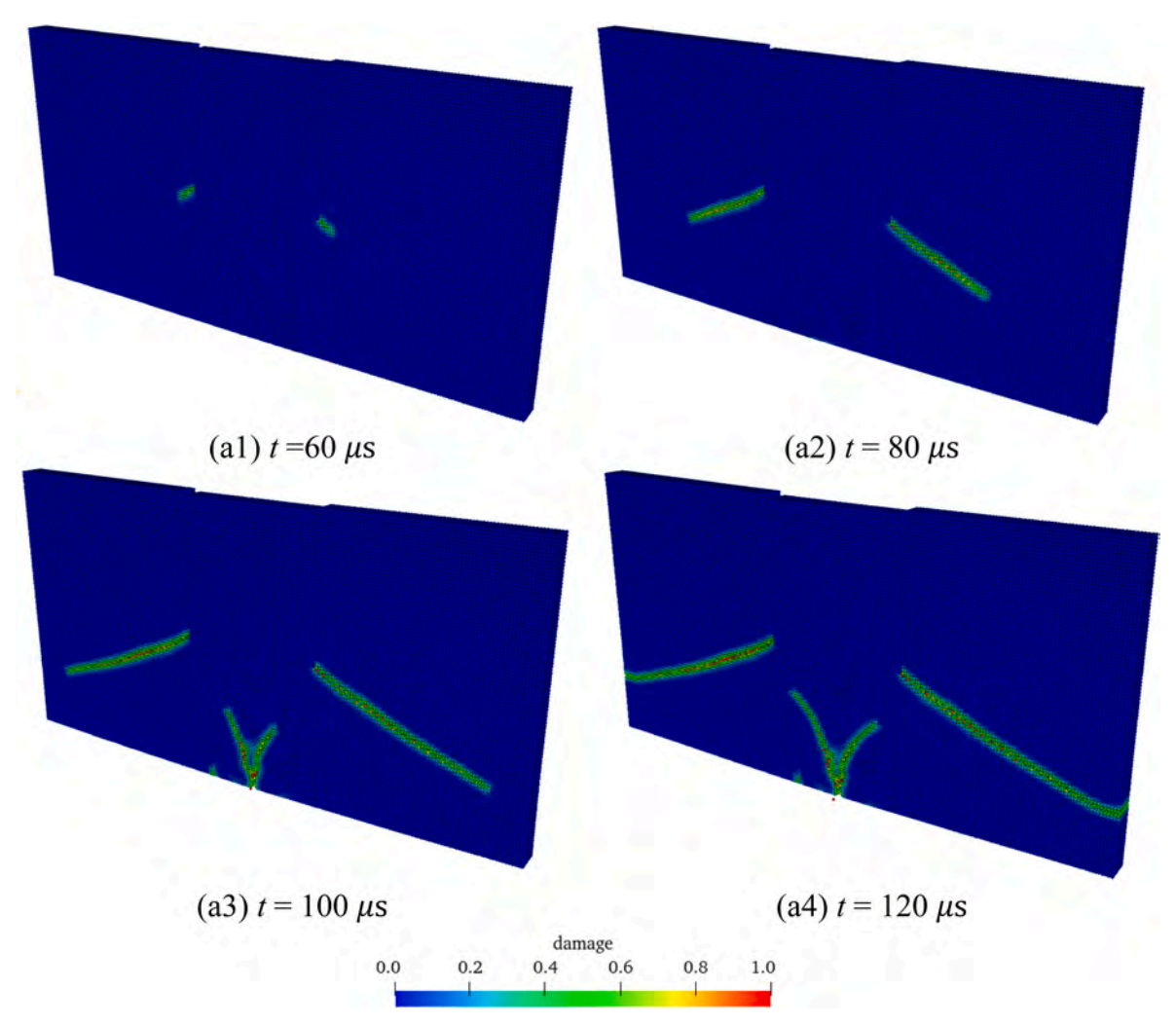


Fig. 17. Damage process simulated by OSB-PD - Kalthoff-Winkler impact test.

simulate the dynamic responses of sea ice cantilever beams (Cao et al., 2024) and hydro-elastic water entry (Jing et al., 2024). These studies fully demonstrate the feasibility of coupling particle-based fluid methods (e.g., SPH) with PD for fracture-related FSI problems. However, in the above-mentioned SPH-PD methods, the numerical instability and pressure oscillations of the traditional Weakly Compressible SPH (WCSPH) method used to simulate fluids cannot be ignored, which may

significantly affect the initiation and propagation of cracks.

Notably, the incompressible MPS method exhibits high stability in simulating violent flow processes — a key advantage for ensuring accurate fluid load transfer in FSI problems involving fracture. However, there are few studies on coupling MPS with PD, especially for 3D FSI problems involving structural fracture. Considering the high computational cost inherent in 3D FSI numerical simulation, another

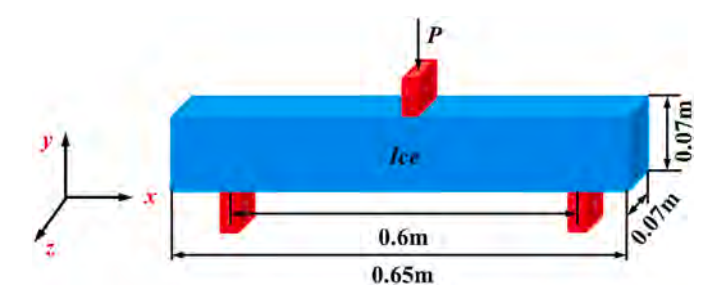
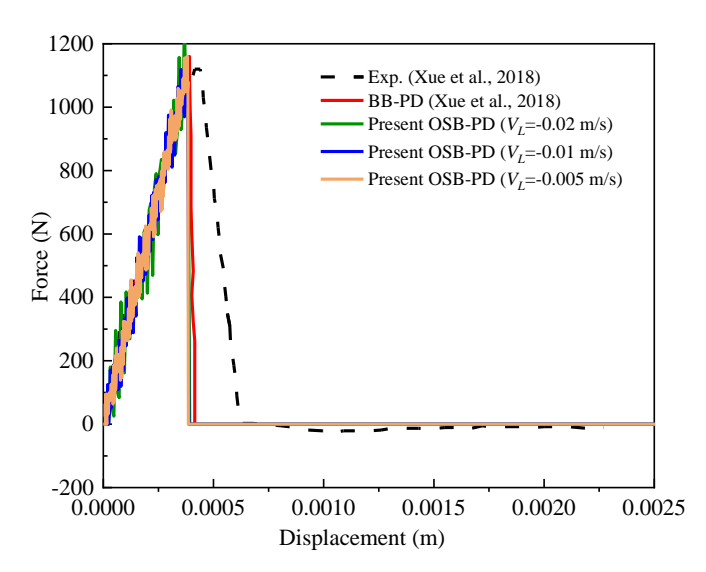


Fig. 18. Schematic of the numerical model - three-point bending of an ice beam.

**Table 5**Parameters in the simulation - three-point bending of an ice beam.

PD parameters	Values
Density (kg/m³)	900
Initial particle spacing (m)	$5  imes 10^{-3}$
Young's modulus (Pa)	$6.83\times10^9$
Poisson's ratio	0.3
Critical energy release rate (J/ m <sup>2</sup> )	19.0
critical bond stretch ratio $s_0$	$3.9\times10^{-4}$
Time step(s)	$2.0\times10^{-6}$



**Fig. 19.** Comparison of force - displacement relationship among the results obtained by experiment(Xue et al., 2018), BB-PD (Xue et al., 2018), and present OSB-PD with different force loading rates - three-point bending of an ice beam.

contribution of this study is to introduce KFBI into the MPS-PD model to achieve multi-resolution simulation.

The remaining parts of this study are organized as follows: Section 2 briefly introduces the improved MPS method, the PD method and their coupling algorithm. Section 3 validates the numerical model through several benchmarks and presents the numerical results of FSI problems with fracture. Section 4 presents the concluding remarks and future perspectives.

#### 2. Numerical methods

## 2.1. MPS method for fluid simulation

The MPS method was first proposed by Koshizuka and Oka (1996) and was initially designed for simulating viscous and incompressible fluids. Its governing equations comprise the mass conservation equation

and the momentum conservation equation, which are given as follows:

$$\frac{D\rho_f}{Dt} + \rho_f \nabla \cdot \mathbf{v} = 0 \tag{1}$$

$$\rho_f \frac{D\mathbf{v}}{Dt} = -\nabla P + \mu_f \nabla^2 \mathbf{v} + \rho_f \mathbf{g}$$
 (2)

where subscript f denotes the MPS fluid particle;  $\rho_f$ , t, v, P,  $\mu_f$ , g represent density, physical time, velocity vector, pressure scalar, dynamic viscosity and gravitational acceleration vector, respectively.

The degree of interaction among MPS particles depends on the kernel function w(r). The kernel function proposed by Zhang et al. (2014), which can significantly suppress non-physical pressure oscillations, is employed. Its specific form is given by:

$$w(r) = \begin{cases} \frac{r_e}{0.85r + 0.15r_e} - 1 & 0 \le r < r_e \\ 0 & r \ge r_e \end{cases}$$
 (3)

where r is the distance between two MPS particles, and  $r_e$  is the influence radius. Specifically,  $r_e$  is set to 2.01  $r_0$  for the gradient model and 4.1  $r_0$  for the Laplacian model, where  $r_0$  is the initial particle spacing.

To approximate physical interactions between particles, numerical constructs such as gradient, divergence, and Laplacian models are employed as discrete operators in the particle method. Their specific definitions are given by:

$$\langle \nabla \phi \rangle_i = \frac{d}{n^0} \sum_{i \neq i} \frac{\phi_j + \phi_i}{|\mathbf{r}_i - \mathbf{r}_i|^2} (\mathbf{r}_j - \mathbf{r}_i) w(|\mathbf{r}_j - \mathbf{r}_i|)$$
(4)

$$\langle \nabla \cdot \mathbf{\Phi} \rangle_i = \frac{d}{n^0} \sum_{j \neq i} \frac{(\mathbf{\Phi}_j - \mathbf{\Phi}_i) \cdot (\mathbf{r}_j - \mathbf{r}_i)}{|\mathbf{r}_i - \mathbf{r}_i|^2} w(|\mathbf{r}_j - \mathbf{r}_i|)$$
(5)

$$\langle \nabla^2 \phi \rangle_i = \frac{2d}{n^0 \lambda} \sum_{j \neq i} (\phi_j - \phi_i) w(|\mathbf{r}_j - \mathbf{r}_i|)$$
 (6)

$$\lambda = \frac{\sum_{j \neq i} w(|\mathbf{r}_j - \mathbf{r}_i|) |\mathbf{r}_j - \mathbf{r}_i|^2}{\sum_{j \neq i} w(|\mathbf{r}_j - \mathbf{r}_i|)}$$
(7)

where subscript i and j denote particle i and its neighbor particle j,  $\phi$  is the physical scalar of MPS particles,  $\mathbf{r}$  is the position vector relative to the origin,  $\mathbf{\Phi}$  is the physical vector, d is the number of space dimensions,  $n^0$  is the initial particle density,  $\lambda$  is a parameter that serves to ensure the increase in variance matches the analytical solution.

For the MPS method, the pressure field is obtained by solving the Poisson Pressure Equation (PPE). The present work adopts the mixed source term method (Khayyer and Gotoh, 2011; Tanaka and Masunaga, 2010), which balances both stability and accuracy, and its expression is given by:

$$\langle \nabla^2 p^{k+1} \rangle_i = (1 - \gamma) \frac{\rho_f}{\Delta t} \nabla \cdot \mathbf{u}_i^* - \gamma \frac{\rho_f}{\Delta t^2} \frac{\langle n^k \rangle_i - n^0}{n^0}$$
 (8)

where  $p^{k+1}$  is the pressure at step k+1,  $\Delta t$  is the time step,  $\mathbf{u}_i^*$  is the intermediate velocity,  $\langle n^k \rangle_i$  is the intermediate particle density, and  $\gamma$  is a blending parameter, with its value set to 0.01 in the present work.

The free surface detection method, which relies on the asymmetric distribution of neighboring particles, is adopted in the present work, given by:

$$\langle n \rangle_i^* \langle \beta n_0 \tag{9}$$

$$\langle \mathbf{F} \rangle_i = \frac{d}{n^0} \sum_{j \neq i} \frac{(\mathbf{r}_j - \mathbf{r}_i)}{|\mathbf{r}_j - \mathbf{r}_i|} w(|\mathbf{r}_j - \mathbf{r}_i|)$$
(10)

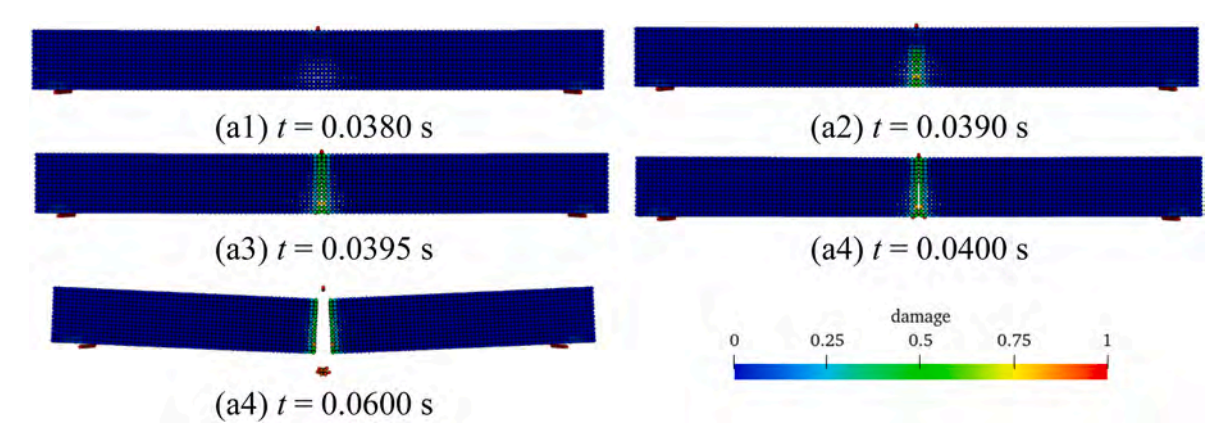


Fig. 20. Fracture process of ice beam simulated by PD ( $V_L = -0.01 \text{ m/s}$ ) - three-point bending of an ice beam.

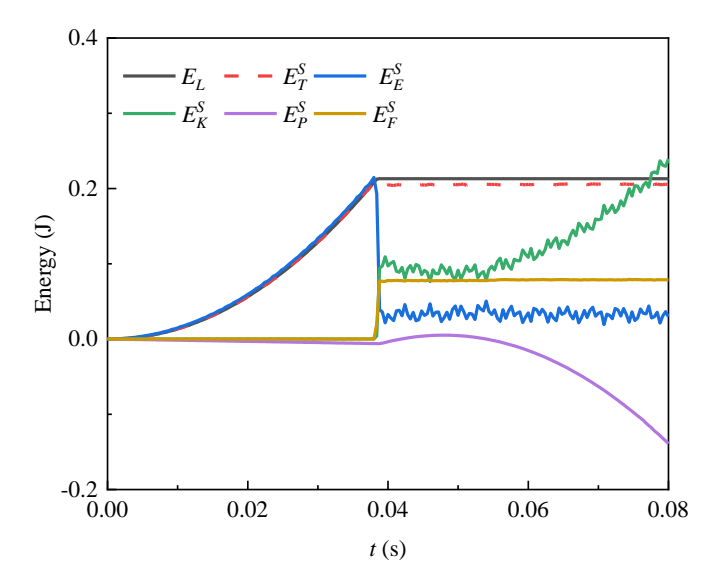


Fig. 21. Time histories of different energies ( $V_{\rm L}=-0.01~{\rm m/s}$ ) - three-point bending of an ice beam.

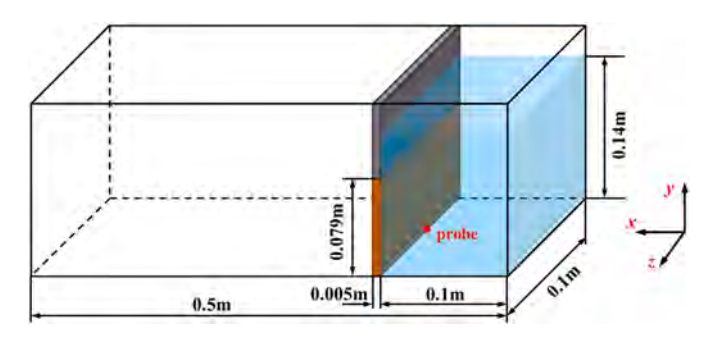


Fig. 22. Schematic of the numerical model - deformation of an elastic gate induced by flood discharge.

$$\langle \mathbf{F} \rangle_i > \alpha |\mathbf{F}^0| \tag{11}$$

where **F** is defined as the vector that characterizes the asymmetric distribution of MPS neighboring particles, and  $|\mathbf{F}^0|$  is defined as the  $\langle \mathbf{F} \rangle_i$  value corresponding to the initial distribution of internal fluid particles. Parameters  $\beta$  and  $\alpha$  are assigned values of 0.8 and 0.9, respectively. Fig. 1 presents the schematic of the free surface detection. It can be observed that when fluid particles are inside the fluid, the  $\langle \mathbf{F} \rangle_i$  is

**Table 6**Parameters in the simulation - deformation of an elastic gate induced by flood discharge.

MPS parameters	Values	PD parameters	Values
Density (kg/m³) Initial particle spacing (m)	$1000 \\ 1.25 \times \\ 10^{-3}$	Density (kg/m³) Initial particle spacing (m)	$1100$ $1.25 \times 10^{-3}, 1.0 \times 10^{-3},$ $10^{-3},$ $8.33 \times 10^{-4}, 6.25 \times 10^{-4}$
Viscosity (Pa·s)	$\begin{array}{c} 8.9 \times \\ 10^{-5} \end{array}$	Young's modulus (Pa)	$8.0  imes 10^6$
Time step (s)	$\begin{array}{c} 2.5 \times \\ 10^{-4} \end{array}$	Poisson's ratio	0.4
-	-	Time step (s)	$5.0\times10^{-6}$

relatively small due to the relatively uniform distribution of surrounding particles. In contrast, when fluid particles are on the free surface, there are no particles outside the free surface, and this uneven distribution leads to a significantly larger value of  $\langle F \rangle_i$ .

The time step of the MPS method needs to satisfy the Courant-Friedrichs-Lewy (CFL) condition, which is given by:

$$\Delta t_{\rm mps} < \frac{Cdp}{\nu_{\rm max}} \tag{12}$$

where  $\Delta t_{\rm mps}$  and dp represent the time step of the MPS method and the initial particle spacing, respectively.  $v_{\rm max}$  represents the maximum velocity of the field, and for dam-break cases, it is generally estimated to take the form  $v_{\rm max} = \sqrt{2gh}$ . C is set to 0.5 in this study.

### 2.2. Ordinary state-based PD for structure simulation

PD is mainly categorized into three types: Bond-Based PD (BB-PD), Ordinary State-Based PD (OSB-PD), and Non-Ordinary State-Based PD (NOSB-PD). BB-PD, which is the simplest model, relies on pairwise particle bonds but suffers from a fixed Poisson's ratio (0.25) for isotropic materials and limited applicability to only brittle materials, restricting its engineering utility. While NOSB-PD suffers from zero-energy modes and numerical instability generated by non-local deformation gradient computation. In contrast, OSB-PD achieves an optimal balance between adaptability, simulation precision, and result stability—making it particularly suited for this study's focus on analyzing fluid-fracture coupling problems (Li et al., 2022).

The equation of motion for PD particles in structures is derived based on Newton's second law, expressed as:

$$\rho_a \ddot{\mathbf{u}}_a = \int_{\mathbb{R}_\delta} \left[ \underline{\mathbf{T}}_a[\mathbf{x}_a, t] \langle \mathbf{x}_b - \mathbf{x}_a \rangle - \underline{\mathbf{T}}_b[\mathbf{x}_b, t] \langle \mathbf{x}_a - \mathbf{x}_b \rangle \right] dV_b + \rho_a \mathbf{g} + \frac{\mathbf{F}_a^{\text{ext}}}{V_a}$$
(13)

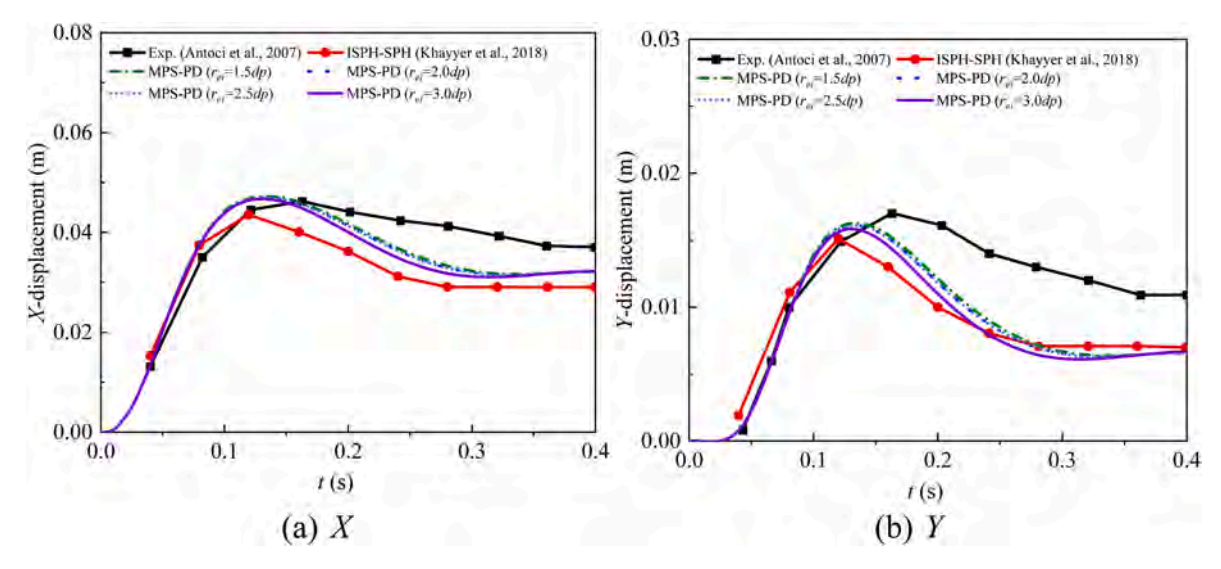


Fig. 23. Comparison of displacement time histories among the results obtained by experiment (Antoci et al., 2007), ISPH-SPH (Khayyer et al., 2018), and MPS-PD with different interpolation radii (dp/dx = 1.5) - deformation of an elastic gate induced by flood discharge.

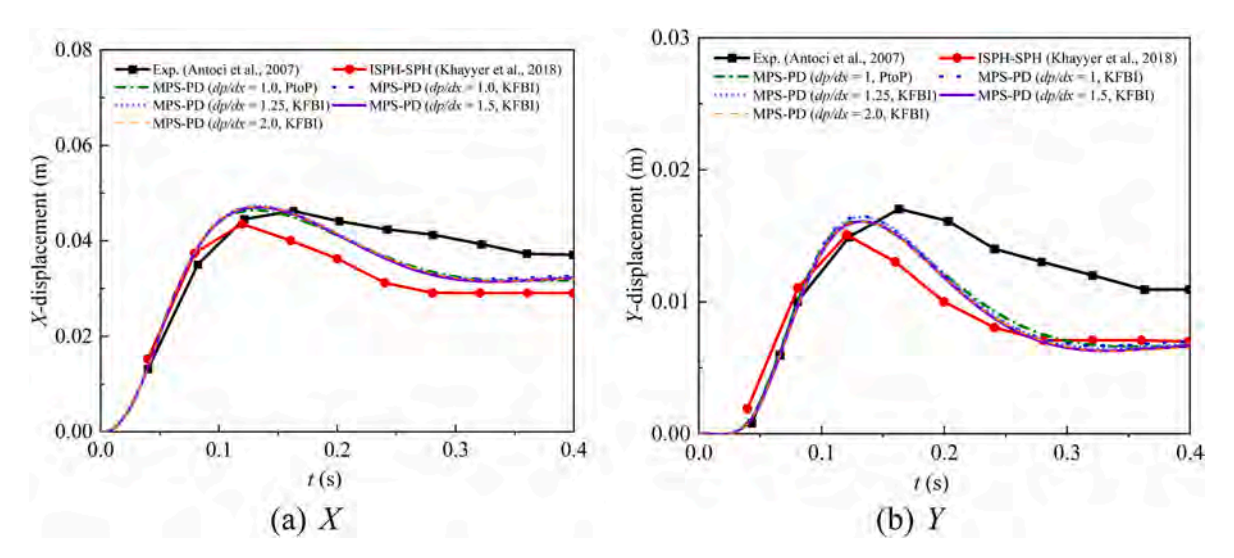


Fig. 24. Comparison of displacement time histories among the results obtained by experiment (Antoci et al., 2007), ISPH-SPH (Khayyer et al., 2018), and MPS-PD with different resolutions ( $r_{ei} = 2dp$ ) - deformation of an elastic gate induced by flood discharge.

where subscripts a and b denote the PD structural particles,  $\ddot{\mathbf{u}}_a$  is the acceleration vector,  $\mathbf{x}$  is the initial relative position, the  $\mathbb{R}_\delta$  is the influence region of PD particles, defined as  $\mathbb{R}_\delta = \{\mathbf{x}_b : |\mathbf{x}_b - \mathbf{x}_a| < \delta\}$  with  $\delta$  being 3.015dx in the present work.  $\underline{\mathbf{T}}$  denotes the force density vector, V is the volume of PD particle,  $\rho_a\mathbf{g}$  is the body force per unit volume,  $\mathbf{F}_a^{\mathrm{ext}}$  is external force exerted on the PD particles, consisting of fluid force and boundary force in this study.

The force density vector  $\underline{\mathbf{T}}$  is given by:

$$\underline{\mathbf{T}}[\mathbf{x}_a, t]\langle \mathbf{x}_b - \mathbf{x}_a \rangle = \underline{t}[\mathbf{x}_a, t]\langle \mathbf{x}_b - \mathbf{x}_a \rangle \underline{\mathbf{M}}$$
(14)

where  $\underline{t}$  is the force density scalar state, and  $\underline{\mathbf{M}}$  is the unit deformation vector state. In 3-D problems, their specific expressions are given by:

$$\underline{t}[\mathbf{x}_a, t]\langle \mathbf{x}_b - \mathbf{x}_a \rangle = 3k \frac{wx}{m} \theta + \alpha \underline{w} \underline{e}^d$$
(15)

$$\underline{\mathbf{M}} = \frac{(\mathbf{x}_b - \mathbf{x}_a) + (\mathbf{u}_b - \mathbf{u}_a)}{|(\mathbf{x}_b - \mathbf{x}_a) + (\mathbf{u}_b - \mathbf{u}_a)|}$$
(16)

where k' and  $\alpha$  are positive constants,  $\underline{w}$  is the influence function and  $\underline{w}$  =

$$\left(1-\frac{(\mathbf{x}_b-\mathbf{x}_a)^2}{\delta^2}\right)^2$$
 (Huang et al., 2015) is employed in the present study,  $m$ 

is the weighted volume,  $\theta$  and  $\underline{e}^d$  are the volume dilatation and deviatoric extension state,  $\mathbf{u}$  is the displacement vector of a PD particle. In 3D problems, the parameters mentioned above can be given by:

$$\begin{cases} k' = k, \alpha = \frac{15\mu}{m} \\ m = \int_{\mathbb{R}_{\delta}} \underline{w} ||\mathbf{x}_b - \mathbf{x}_a||^2 dV_b \\ \theta = \frac{3}{m} \int_{\mathbb{R}_{\delta}} (\underline{w} \underline{x} \underline{e}) dV_b, \ \underline{e}^d = \underline{e} - \frac{\theta \underline{x}}{3} \end{cases}$$
(17)

where k and  $\mu$  represent the bulk modulus and shear modulus of the material, respectively,  $\underline{e}$  is the elongation scalar state(Yao et al., 2023), expressed as:

$$\underline{e} = y\langle \mathbf{x}_b - \mathbf{x}_a \rangle - \underline{x}\langle \mathbf{x}_b - \mathbf{x}_a \rangle \tag{18}$$

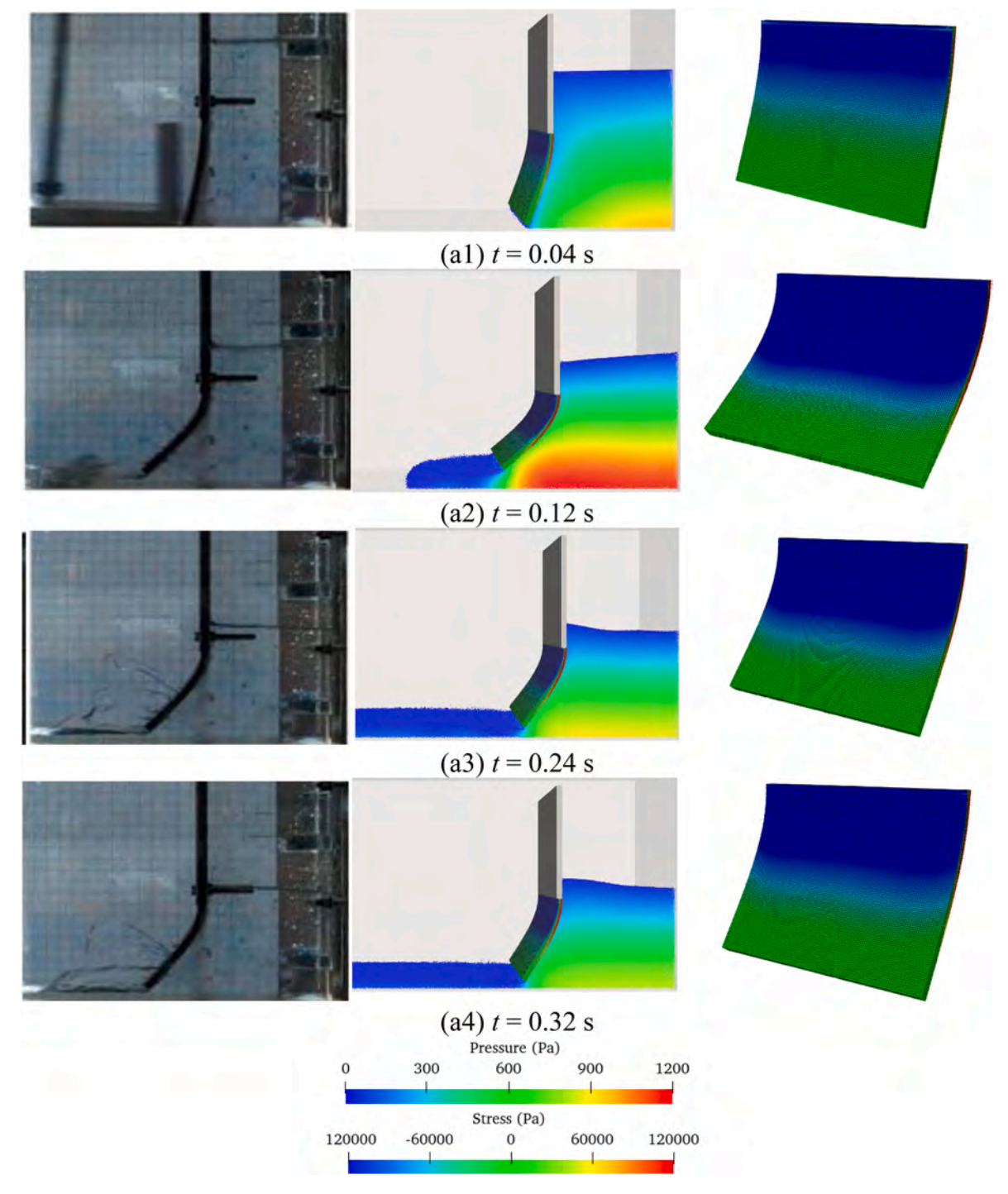


Fig. 25. Comparison of the discharge flood morphology and structural deformation between experimental snapshots (Antoci et al., 2007) and numerical results obtained by the present 3D MPS-PD solver-deformation of an elastic gate induced by flood discharge.

where  $\underline{x}$  and  $\underline{y}$  are the initial distance and the current distance between neighboring particles, respectively.

When the bond length between neighboring PD particles exceeds the critical value  $s_0$ , the force density generated by their interaction will disappear, which is an irreversible process. The function  $\varphi_{ab}$ , which is utilized to describe the interaction state between neighboring PD particles, is given by:

$$\varphi_{ab} = \begin{cases} 1, \text{if } s < s_0 \\ 0, \text{elsewhere} \end{cases}$$
 (19)

where s is the scalar bond stretch between neighboring PD particles, which is given by,

$$s = \frac{|(\mathbf{x}_b - \mathbf{x}_a) + (\mathbf{u}_b - \mathbf{u}_a)| - |(\mathbf{x}_b - \mathbf{x}_a)|}{|(\mathbf{x}_b - \mathbf{x}_a)|}$$
(20)

The critical stretch  $s_0$  (Madenci and Oterkus, 2014) is given by:

$$s_0 = \sqrt{\frac{G_0}{\left(3\mu + \left(\frac{3}{4}\right)^4 \left(k - \frac{5}{3}\mu\right)\right)\delta}}$$
(21)

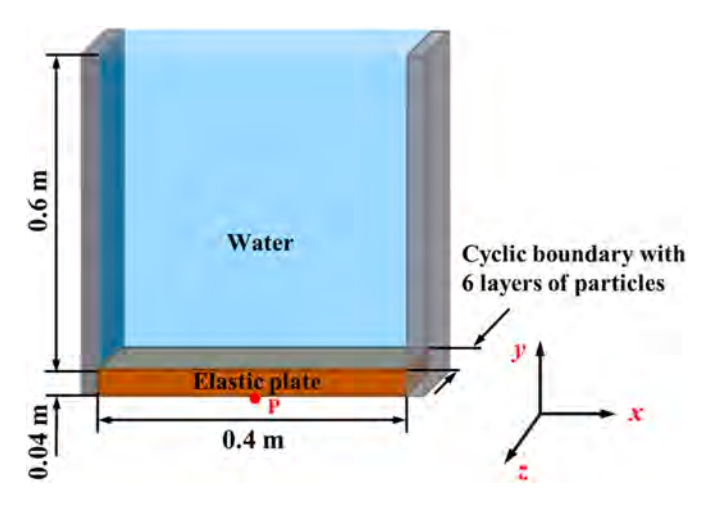


**Fig. 26.** Schematic of the numerical model - deformation of an elastic plate induced by a hydrostatic water column.

**Table 7**Parameters in the simulation - deformation of an elastic plate induced by a hydrostatic water column.

MPS parameters	Values	PD parameters	Values
Density (kg/ m³) Initial particle spacing (m)	1000 1.0 × 10 <sup>-2</sup>	Density (kg/m³) Initial particle spacing (m)	2700 $1.0 \times 10^{-2}$ , $8.0 \times 10^{-3}$ , $6.67 \times 10^{-3}$
Viscosity (Pa· s)	$8.9 \times 10^{-5}$	Young's modulus (Pa)	$67.5\times10^9$
Time step (s)	$1.0 \times 10^{-3}$	Poisson's ratio	0.34
-	-	Time step (s)	$2.0\times10^{-6}$

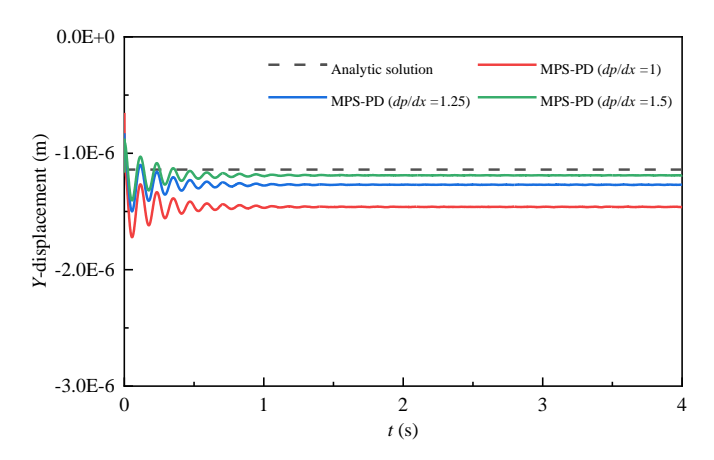


**Fig. 27.** Comparison of displacement time histories of the P probe between the analytic solution and MPS-PD results with different resolutions-deformation of an elastic plate induced by a hydrostatic water column.

where  $G_0$  is the critical energy release rate of the material and  $\delta$  is the horizon.

The selection of PD time step follows the critical value proposed by Zhang and Qiao (2020), given by:

$$\Delta t_{\rm PD} < \sqrt{2\rho_s / \left(\sum_{b \in \Omega_*} 2\alpha \underline{w} V_b\right)}$$
 (22)

where  $\Delta t_{PD}$  is the time step of PD simulation.

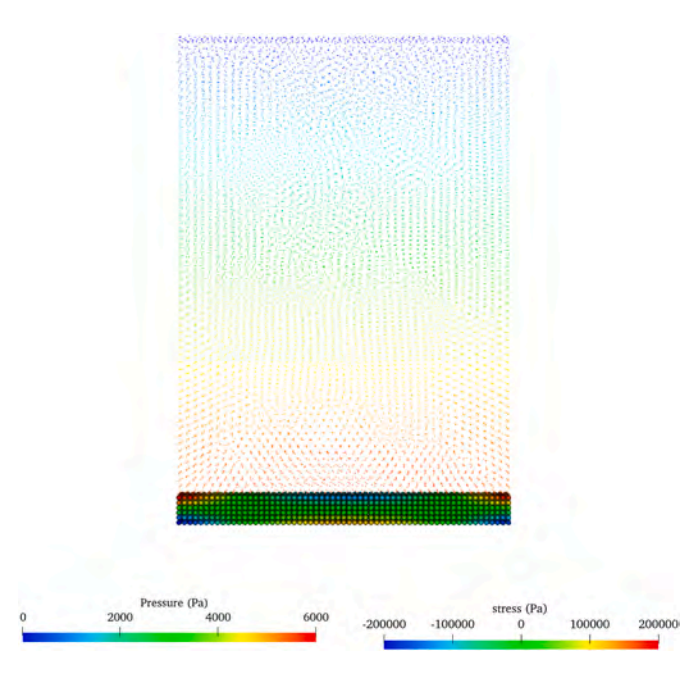


**Fig. 28.** Snapshots of pressure/stress fields at t=4.0 s reproduced by the MPS-PD solver with dp/dx=1.5 - deformation of an elastic plate induced by a hydrostatic water column.

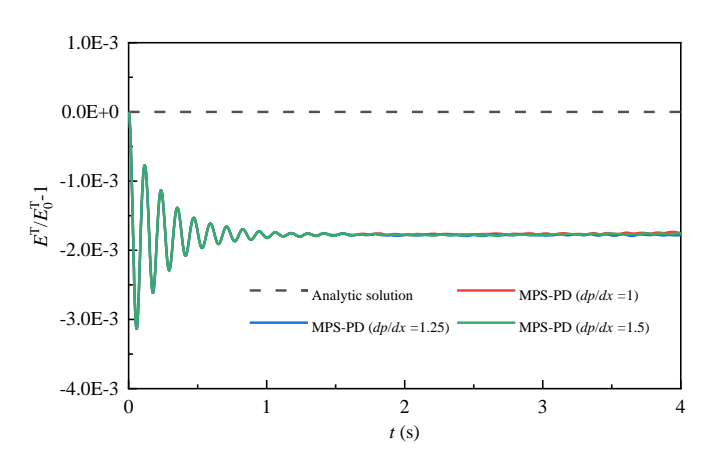


**Fig. 29.** Comparison of time histories of normalized total energies between the analytic solution and MPS-PD results with different resolutions - deformation of an elastic plate induced by a hydrostatic water column.

#### 2.3. Coupling of MPS and PD

In the MPS model, solid boundaries are composed of multiple layers of particles (Xie et al., 2021a). Among these, the pressure of the outermost layer particles (wall particles) that are adjacent to the fluid is obtained by solving the PPE (Zhang and Wan, 2017). For MPS-PD coupling, the simplest method is to discretize the elastic structure using MPS and PD particles with the same resolution, which can be referred to as Point-to-Point (PtoP) coupling. Structural particles possess the characteristics of both MPS particles and PD particles. MPS wall particles transmit the obtained fluid pressure to PD particles; conversely, PD particles transmit displacement and velocity to the MPS structural particles of the elastic structure. The above coupling process can be expressed as:

$$\mathbf{F}^{\text{ext}} = -(P^{s} \Delta S) \mathbf{n} \tag{23}$$

$$\mathbf{u}^{\mathrm{MPS}} = \mathbf{u}^{\mathrm{PD}} \tag{24}$$

Fig. 30. Schematic of the numerical model - deformation of a hanging elastic plate induced by the dam-break flow.

**Table 8**Parameters in the simulation - deformation of a hanging elastic plate induced by the dam-break flow

MPS parameters	Values	PD parameters	Values
Density (kg/ m <sup>3</sup> )	1000	Density (kg/m <sup>3</sup> )	1250
Initial particle spacing	$1.75 \times$	Initial particle spacing	$1.167 \times$
(m)	$10^{-3}$	(m)	$10^{-3}$
Viscosity (Pa· s)	$8.9\times10^{-5}$	Young's modulus (Pa)	$4.0  imes 10^6$
Time step (s)	$2.5\times10^{-4}$	Poisson's ratio	0.4
-	-	Time step (s)	$5.0\times10^{-6}$

$$\mathbf{v}^{\text{MPS}} = \mathbf{v}^{\text{PD}} \tag{25}$$

where  $P^s$  is the pressure exerted on a PD particle,  $\Delta S$  is the force-bearing area of MPS boundary particles,  $\mathbf{n}$  is the normal direction of the boundary.

Several multi-resolution techniques are proposed to improve the efficiency and performance of FSI solvers. For example, the elastic structures and flow fields can be simulated with different resolutions using a multi-resolution particle method (Khayyer et al., 2019, 2021a). Besides, a high-resolution region can be set around the elastic structure. When coarse particles enter this region, they are split into finer particles by means of an Adaptive Particle Refinement (APR) method (Lyu et al., 2023). In the present study, the Kernel Function-Based Interpolation (KFBI) technique is introduced into the MPS-PD solver. This technique previously was utilized and validated in 3D MPS-FEM solver (Zhang et al., 2022a), 2D SPH-Phase Field solver (Rahimi and Moutsanidis, 2023), and 2D SPH-PD solver (Rahimi et al., 2022). The schematic of the KFBI technique is presented in Fig. 2. The pressure exerted on the PD particles on the structural surface is obtained by interpolating the pressure of MPS wall particles within their influence domain, given by:

$$P_a^S = \frac{\sum\limits_i P_i \mathbf{n}_i W(|\mathbf{r}_i - \mathbf{r}_a|)}{\sum\limits_i W(|\mathbf{r}_i - \mathbf{r}_a|)} \tag{26}$$

The displacement and velocity of MPS structural particles are, in turn, obtained by interpolating the displacement and velocity of PD particles, which are given by:

$$\mathbf{u}_{i} = \frac{\sum_{a} \mathbf{u}_{a} W(|\mathbf{r}_{a} - \mathbf{r}_{i}|)}{\sum_{a} W(|\mathbf{r}_{a} - \mathbf{r}_{i}|)}$$
(27)

$$\mathbf{v}_{i} = \frac{\sum_{a} \dot{\mathbf{u}}_{a} W(|\mathbf{r}_{a} - \mathbf{r}_{i}|)}{\sum_{a} W(|\mathbf{r}_{a} - \mathbf{r}_{i}|)}$$
(28)

Particle treatment near the fracture surface is shown in Fig. 3. When the structure fractures, MPS structural particles only interact with PD structural particles on the same side of the fracture surface. To prevent

the penetration of fluid particles, when fluid particles approach the ghost particles at the fracture surface, these ghost particles are directly converted into wall particles and participate in solving the PPE.

The flow chart of the in house MPSPD-SJTU solver is presented in Fig. 4. Since the MPS method employed in this study is a semi-implicit solution, while the OSB-PD is an explicit solution, the time step of MPS can be larger than that of PD to balance the stability and efficiency of the MPS-PD solver. The Modified Serial Staggered (MSS) strategy (Sun et al., 2021) is employed, and under this strategy, the PD solver iterates several times within one MPS iteration loop. After the structure fractures, the fragments may collide with the wall boundary. Therefore, in addition to the PD force and FSI force, the DEM model is also invoked to calculate the contact force. The calculation of contact forces has been described in detail in our previous work (Xie et al., 2021b, 2025), and will not be repeated here.

# 3. Numerical results

#### 3.1. Validation of MPS model

In this section, the accuracy of the MPS solver is first verified. The MPS solver is utilized to simulate dam-break flow impacting a fixed square obstacle, which has been studied experimentally by Kleefsman et al. (2005). The schematic of the numerical model is presented in Fig. 5. The dimensions of the numerical tank are  $3.22~\text{m}\times1.0~\text{m}\times1.0~\text{m}$ .

A water column of 1.228 m  $\times$  0.1 m  $\times$  0.55 m is located on the right side of the water tank. A square obstacle with dimensions of 0.161 m  $\times$  0.403 m  $\times$  0.161 m is placed on the central axis of the water tank, 0.744 m away from the right wall of the tank. A pressure probe (marked as P1) is installed on the square obstacle, and a wave height probe (marked as H1) is installed at the bottom of the water tank. Other numerical parameters are listed in Table 1.

Fig. 6 and Fig. 7 show the pressure and wave height time histories measured by the P1 and H1 probes. It can be noted that the MPS results converge well to the experimental data as the resolution is refined. Besides, the high-resolution MPS results all show good agreement with both the SPH simulation results (Sun et al., 2015) and the experimental data (Kleefsman et al., 2005) in terms of peak values and overall trends.

Fig. 8 shows the snapshots obtained respectively from the experiment and the MPS simulation. It can be seen that the MPS method can accurately describe the shape of the free surface of dam-break flow and capture the droplet splashing phenomenon during the impact process. This comprehensive comparison fully verifies the reliability and accuracy of the MPS method in simulating dam-break flow-related problems.

#### 3.2. Validations of OSB-PD model

#### 3.2.1. Dynamic response of an oscillating cantilever beam

An oscillating cantilever beam is first simulated to validate the ac-

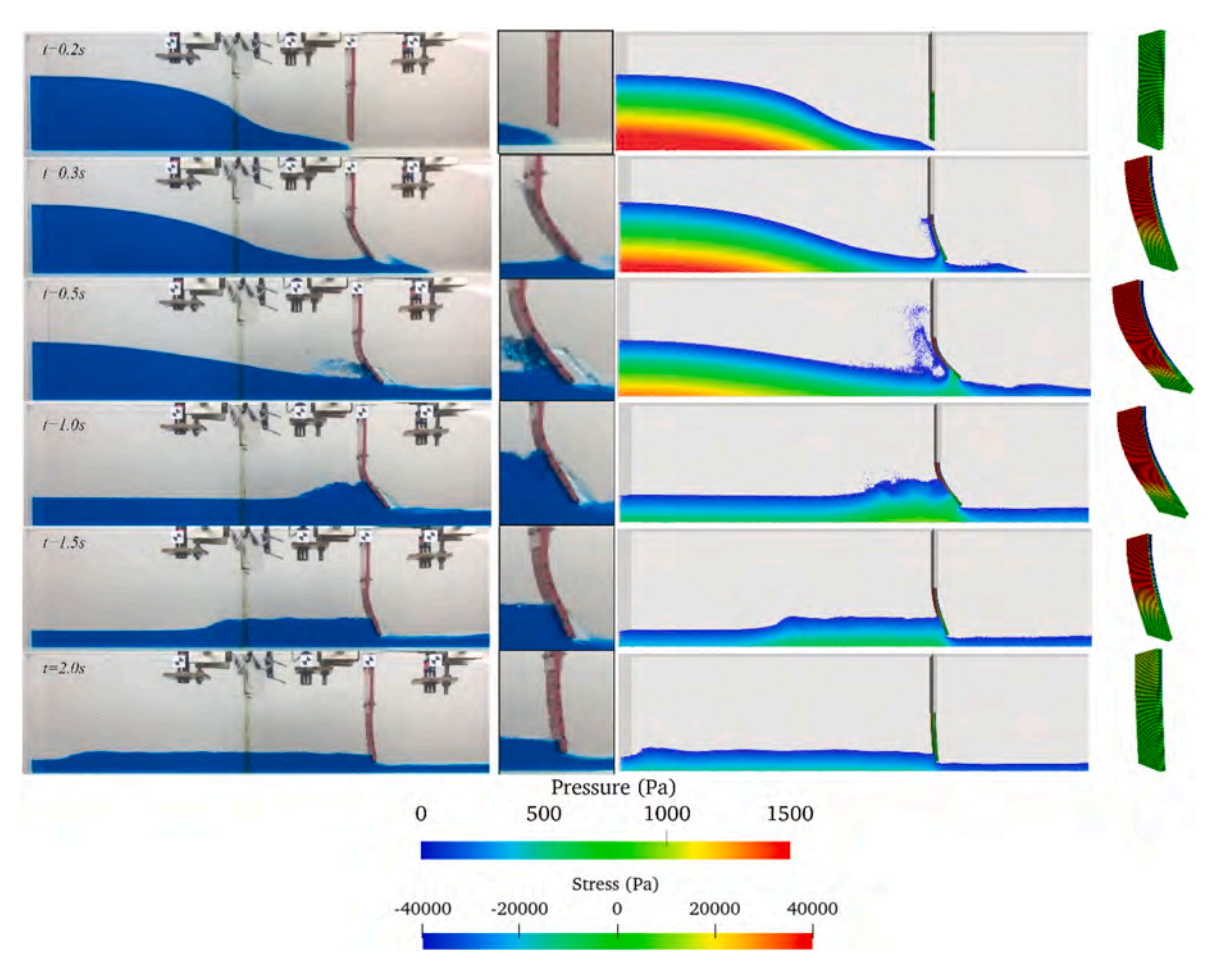


Fig. 31. Comparison of the dam-break flow morphologies and structural deformations at different instants between experimental snapshots (Yilmaz et al., 2021) and numerical results obtained by the present 3D MPS-PD solver - deformation of a hanging elastic plate induced by the dam-break flow.

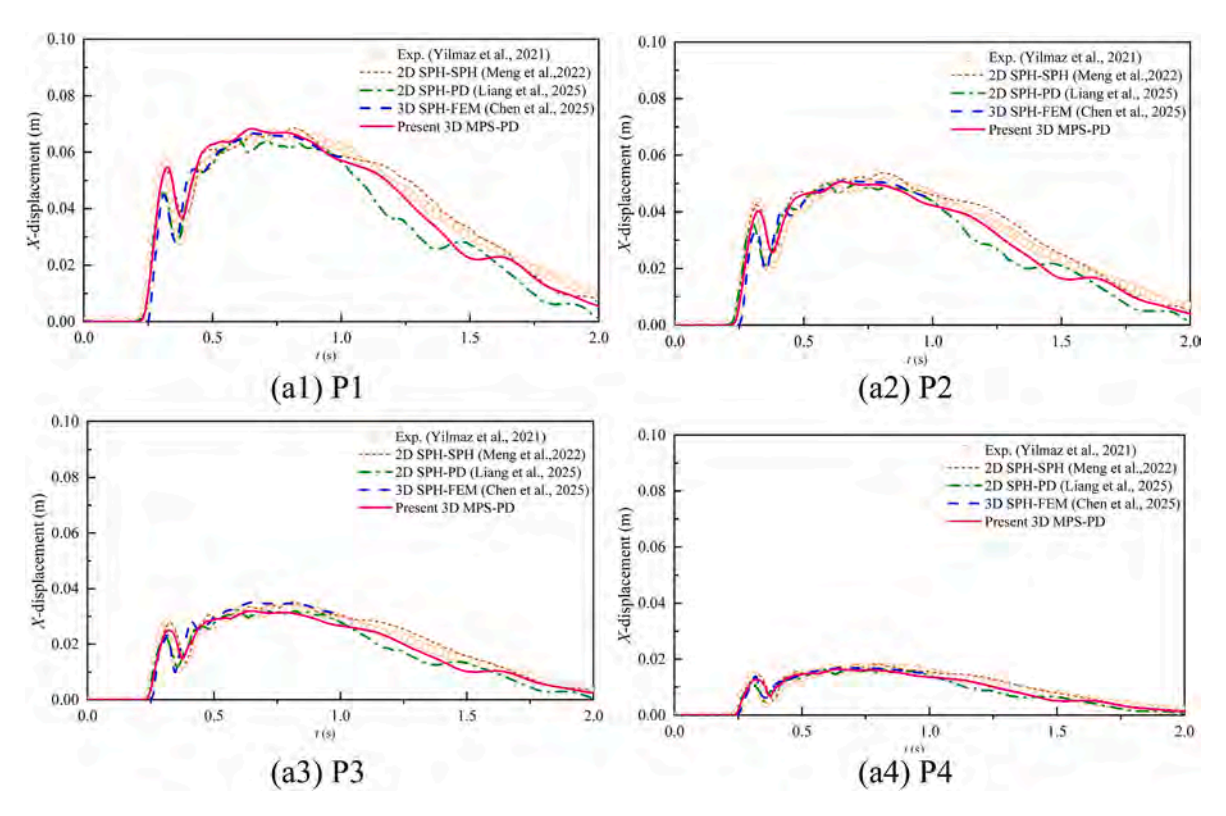
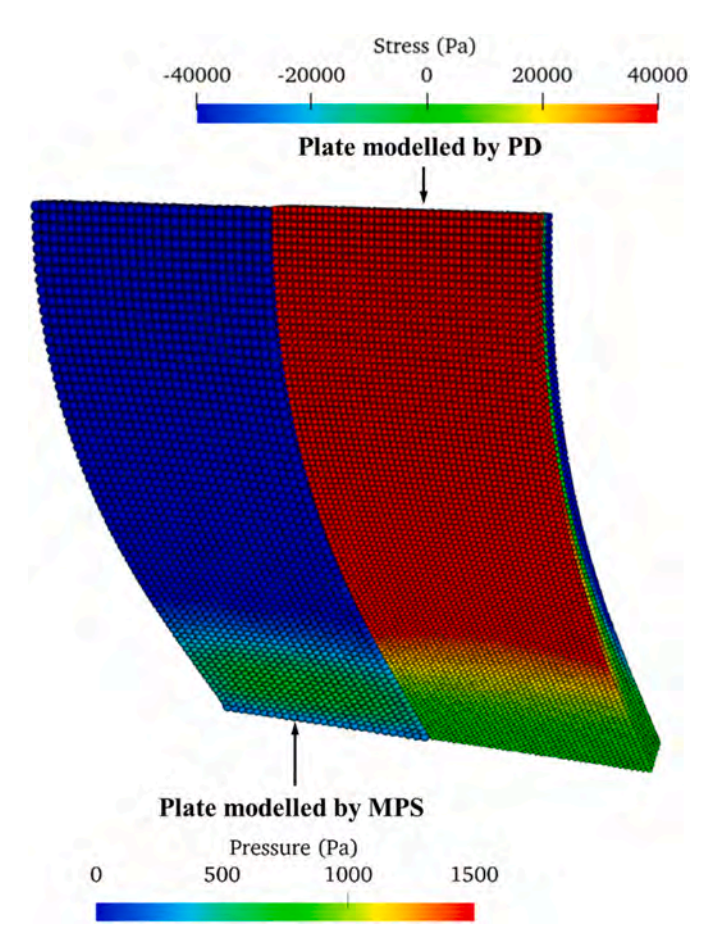
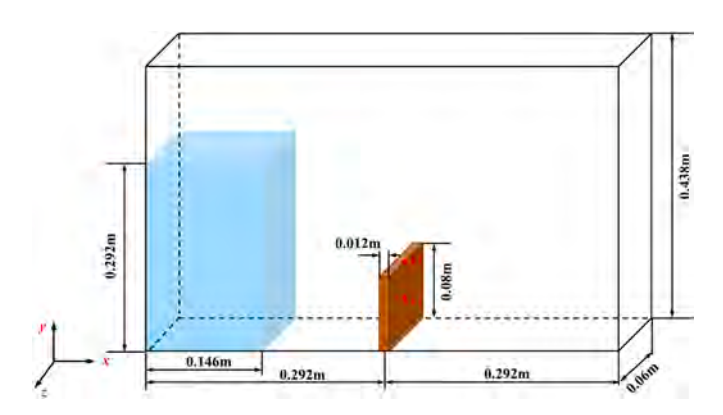


Fig. 32. Comparison of horizontal displacement time histories among the results obtained by experiment (Yilmaz et al., 2021), 2D SPH-SPH (Meng et al., 2022), 2D SPH-PD (Liang et al., 2025a), 3D SPH-FEM (Chen et al., 2025), and the present 3D MPS-PD - deformation of a hanging elastic plate induced by the dam-break flow.



**Fig. 33.** Comparison of plate deformation results modelled by MPS and PD - deformation of a hanging elastic plate induced by the dam-break flow.



 $\begin{tabular}{ll} \textbf{Fig. 34.} Schematic of the numerical model - fracture of an elastic baffle induced by the dam-break flow. \\ \end{tabular}$ 

curacy of the PD part in the MPS-PD solver. The sketch of this numerical model is presented in Fig. 9. The cantilever beam has a length of  $0.2\,\mathrm{m}$ , a width of  $0.01\,\mathrm{m}$ , and a height of  $0.02\,\mathrm{m}$ . A displacement probe is installed at the centroid of the free end. At the initial moment, the cantilever beam is undeformed and in an initial equilibrium position. The initial vertical velocity distribution acting on this beam is given by:

$$v_{y}(x) = v_{y}(L)c_{0}\frac{f(x)}{f(L)}$$
(29)

$$f(x) = (\cos(kL) + \cosh(kL))(\cosh(kx) - \cos(kx)) + (\sin(kL))$$

$$- \sinh(kL))(\sinh(kx) - \sin(kx))$$
(30)

**Table 9**Parameters in the simulation - fracture of an elastic baffle induced by the dambreak flow

MPS parameters	Values	PD parameters	Values
Density (kg/m <sup>3</sup> )	1000	Density (kg/m <sup>3</sup> )	2500
Initial particle spacing (m)	$\begin{array}{c} 2.0 \times \\ 10^{-3} \end{array}$	Initial particle spacing (m)	$1.5\times10^{-3}$
Viscosity (Pa·s)	$\begin{array}{c} 8.9 \times \\ 10^{-5} \end{array}$	Young's modulus (Pa)	$1.0\times10^6$
Time step (s)	$\begin{array}{c} 2.5 \times \\ 10^{-4} \end{array}$	Poisson's ratio	0.0
-	-	Critical energy release rate	$6.07\times10^3,$
		$(J/m^2)$	97.9
-	_	Critical bond stretch ratio $s_0$	1.0, 0.127
-	-	Time step (s)	$5.0\times10^{-6}$

where  $v_y(L) = 0.01 \text{m/s}$  is the initial velocity of the cantilever beam's free end. For the fundamental mode, the value of kL is set to 1.875.  $c_0$  is the sound speed and can be calculated as:

$$c_0 = \sqrt{K_s/\rho_s} = \sqrt{E_s/(3(1-2v)\rho_s)}$$
 (31)

where  $K_s$  is the bulk modulus,  $E_s$  is the Young's modulus, v is the Poisson's ratio, and  $\rho_s$  is the density of the cantilever beam. Other numerical parameters can be found in Table 2.

The vertical displacement time histories of the probe are presented in Fig. 10. The detailed derivation of the analytical solution can be found in the literature (Khayyer et al., 2022b). It can be observed that the results with high resolution are slightly closer to the analytical solution. In general, the PD numerical simulation results with different resolutions are in good agreement with the analytical results in terms of both phase and peak value, which implies that the present PD solver exhibits good convergence characteristics. Besides, the stress distribution, as shown in Fig. 11, is smooth and matches well with deformation.

# 3.2.2. Static deflection of a clamped-clamped elastic beam under uniform load

The accuracy and stability of the PD solver are further investigated by simulating a clamped-clamped beam under uniform load, which has been utilized to validate the SPH structural solver by Khayyer et al. (2022b). The schematic of the numerical model is shown in Fig. 12. The beam has a length of 0.2 m, a width of 0.012 m, and a height of 0.012 m. A deflection probe is installed at the centroid of the bottom of the beam. A uniform load  $q=20\mathrm{N/m^2}$  is applied to the top surface of the beam. Other numerical parameters are presented in Table 3.

Vertical displacement time histories measured by the probe are presented in Fig. 13. The analytic solution is obtained based on the Euler-Bernoulli beam theory and the detailed derivation process can be found in the referenced literature (Khayyer et al., 2022b). The displacement time histories obtained by PD eventually stabilize at a constant value after a brief oscillation. It can be observed that the deflections from simulations with different resolutions are very close to one another, and among these simulations, the deflection from the high-resolution simulation is the closest to the analytic solution. The stress field is very smooth and continuous, as shown in Fig. 14.

#### 3.2.3. Kalthoff-Winkler impact test

The Kalthoff-Winkler impact test is a well-known benchmark case (Kalthoff, 2000), which has been widely used to verify the accuracy of the PD solver in simulating fracture problems. Fig. 15 shows the schematic of the numerical model. There is a steel plate with a length of 0.2 m, a height of 0.1 m, and a width of 0.09 m. Two prefabricated cracks (each 0.05 m in length) extend inward from the upper edge of the steel plate, with a distance of 0.05 m between them. A cylinder with a height of 0.05 m and a diameter of 0.05 m impacts the area between the prefabricated cracks on the top of the steel plate at a velocity of 32 m/s in

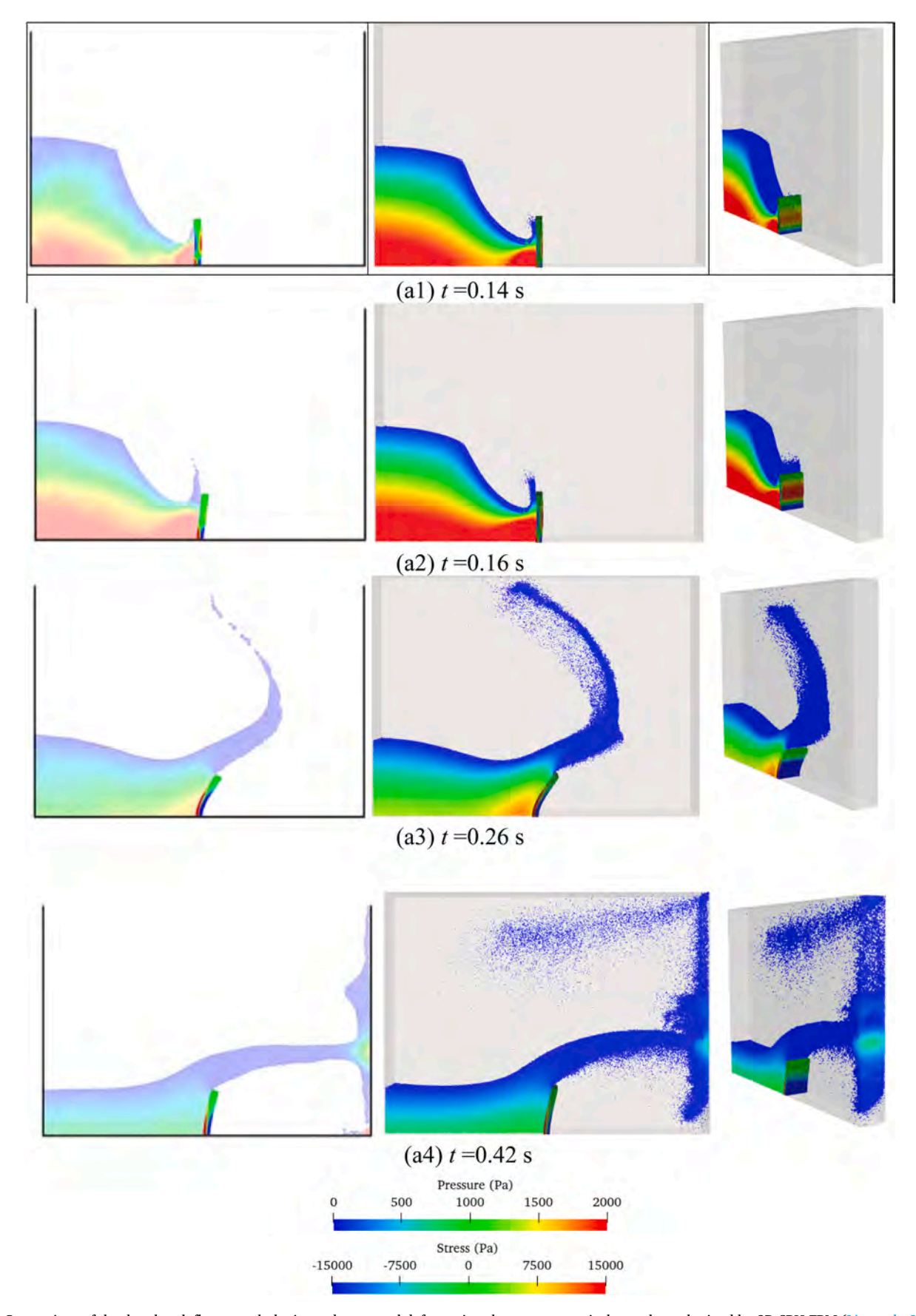
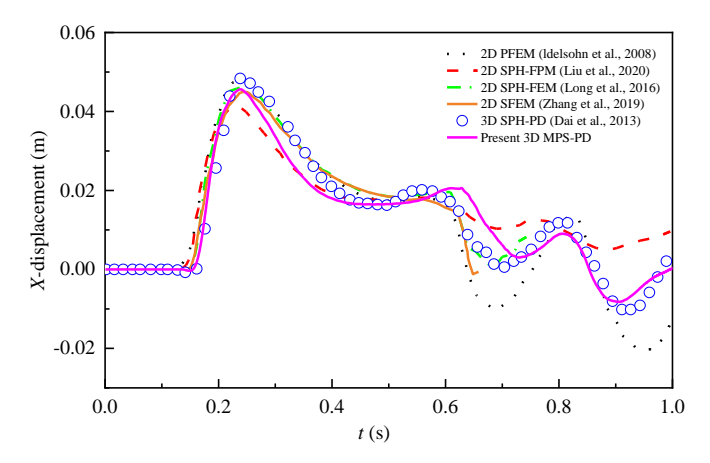


Fig. 35. Comparison of the dam-break flow morphologies and structural deformations between numerical snapshots obtained by 2D SPH-FPM (Liu et al., 2020) and those by the present 3D MPS-PD - fracture of an elastic baffle induced by the dam-break flow.



**Fig. 36.** Comparison of horizontal displacement time histories of probe A among the numerical results obtained by 2D PFEM (Idelsohn et al., 2008), 2D SPH-FPM (Liu et al., 2020), 2D SPH-FEM (Long et al., 2016), 2D SFEM (Zhang et al., 2019), 3D SPH-PD (Dai et al., 2023), and the present 3D MPS-PD - fracture of an elastic baffle induced by the dam-break flow.

the vertical downward direction. Other numerical parameters can be found in Table 4.

Fig. 16 presents the crack path reproduced by BB-PD and OSB-PD. Specifically, the BB-PD solver used herein was developed by rewriting the Fortran code from Madenci and Oterkus (2014) in C++. It can be observed that the crack morphologies simulated by the BB-PD solver and the OSB-PD solver are very similar. Both solvers have captured two types of cracks: one is the primary crack on the impact side, which is related to the presence of the prefabricated crack; the other is the secondary crack generated on the non-impact side due to the tensile force induced by the deformation of the steel plate. The overall path angles are approximately 113.08° for BB-PD and 113.43° for OSB-PD, respectively. Both values are very close to the experimental value of 110°, and relative errors of these two values are both less than 5%. Fig. 17 presents the damage process simulated by OSB-PD. It can be noticed that the primary crack initiates from the tip of the prefabricated crack and gradually extends to the side edge of the steel plate. The secondary crack gradually propagates from the non-impact side when the steel plate deforms significantly.

#### 3.2.4. Three-point bending of an ice beam

In this section, the three-point bending test on an ice beam (Xue et al., 2018) is simulated, and the accuracy of the PD numerical model is verified from the perspectives of load and energy. The schematic of the numerical model is presented in Fig. 18. An ice sample with a length of 0.65 m, a width of 0.07 m, and a thickness of 0.07 m is placed on two support points with a span of 0.6 m. The loading point P is located at the midspan of the ice and on its upper surface. Simulations are conducted with the loading point P moving downward at velocities  $V_L$  of 0.005 m/s, 0.01 m/s, and 0.02 m/s. Other numerical parameters are listed in Table 5.

Fig. 19 presents the load curves obtained by different approaches. Without any damping added, during the sea ice deformation phase, the load curve obtained by OSB-PD exhibits slight oscillations. Among these, the load curves obtained at loading rates of -0.01 m/s and -0.005 m/s show good agreement, indicating that the loading process in the numerical simulations can be regarded as a quasi-static process (Di, 2015; Xiong et al., 2025). It can be seen that during the ice deformation phase, the slope of the curve obtained by OSB-PD shows good agreement with the experimental results. Furthermore, the peak value of the force obtained by OSB-PD is 1160 N, which is also very close to the experimental value of 1128 N Fig. 20 presents the snapshots of the present OSB-PD simulation. It can be seen that cracks initiate from the bottom at the midspan of the ice, and the ice is eventually split into two parts. The same phenomenon has also been observed in different experiments (Ji

et al., 2011; Ni et al., 2021).

The energy conservation features in the structure domain of the present OSB-PD solver are investigated. Energies need to satisfy:

$$E_L = E_T^S = E_F^S + E_F^S + E_F^S + E_F^S$$
 (32)

where  $E_L$  refers to the work done by the loading point on the structural domain.  $E_E^S$  is the total energy of the structural domain.  $E_E^S$ ,  $E_K^S$ ,  $E_K^S$ , and  $E_F^S$  are elastic strain energy, the kinetic energy, gravitational potential energy, and released fracture energy of structure domain. Different energies can be calculated as:

$$E_{L} = \sum_{N} F_{L}(t) V_{L} \Delta t_{PD}$$
(33)

$$E_K^{\mathcal{S}} = \sum_{a \in \Omega_{\mathcal{S}}} \frac{1}{2} m_a^s |\dot{\mathbf{u}}_a|^2, E_P^{\mathcal{S}} = \sum_{a \in \Omega_{\mathcal{S}}} m_a^{\mathcal{S}} \mathbf{g} \cdot \mathbf{u}_a$$
(34)

$$E_E^{S} = \sum_{a \in \Omega_S} W_a V_a = \sum_{a \in \Omega_S} \left( \frac{1}{2} k' \theta^2 + \frac{\alpha}{2} \sum_{\mathbb{R}_{\delta}} \left( \omega \left( \underline{e}^{\underline{d}} \right)^2 V_b \right) \right) V_a$$
 (35)

$$E_F^{S} = \sum_{a \in \Omega_{S}} \left( \frac{1}{2} a' \theta_1^2 + a' \theta_1 \theta_2 + \frac{\alpha}{2} \sum_{H_1} \left( \underline{\omega x}^2 s_0^2 V_b \right) \right) V_a, a' = k' - \frac{\alpha q}{9}$$
 (36)

where N and  $F_L$  refer to the total number of time steps and the external load, respectively.  $\theta_1$  and  $\theta_2$  are the volume dilatation of the fractured part and the volume dilatation of the unfractured part.  $H_1$  is the region where fracture occurs within the influence domain of PD particle a. The method for calculating released fracture energy was proposed by Wu (2024), which builds upon the approach of Zhang and Qiao (2018) by incorporating the coupling effect of  $\theta_1$  and  $\theta_2$ .

Fig. 21 shows time histories of different energies. As can be seen, during the deformation stage, the total energy of the structural domain is almost consistent with the external work, while a small amount of gravitational potential energy is converted into elastic strain energy. After the ice is completely fractured, the loading point detaches from the ice, the external force no longer does work, and the total energy of the structural field also remains unchanged. This total energy is slightly lower than the total work done by the external force, with a relative error less than 4 %. In general, the present OSB-PD model exhibits good energy conservation performance and can meet the requirements of engineering applications.

The numerical results presented above indicate that the OSB-PD solver exhibits high accuracy and can be further coupled with MPS.

### 3.3. Validations of MPS-PD model

# 3.3.1. Deformation of an elastic gate induced by flood discharge

The accuracy of multi-resolution fluid-structure interpolation will be studied by simulating the flood discharge with an elastic gate, which is a benchmark test carried out by Antoci et al. (2007). The schematic of the numerical model is presented in Fig. 22. There is a water tank with a length of 0.5 m and a width of 0.1 m. A water column with a length of 0.1 m, a width of 0.1 m, and a height of 0.14 m is located on the right side of the tank. There is an elastic gate hung from a rigid wall. The gate is located at the left end of the water column and adjacent to it. The elastic gate has a height of 0.079 m, a width of 0.1 m, and a thickness of 0.005 m. A displacement probe is installed at the center of the bottom end of the elastic gate. At the initial state, the elastic gate is undeformed. As the numerical simulation begins, the elastic gate undergoes deformation under the action of the water pressure. Other numerical parameters are listed in Table 6.

Fig. 23 depicts the X-directional and Y-directional displacements measured by the probe. It can be seen that the displacements in the two directions first rise rapidly and then gradually decrease over time. Overall, the numerical simulation results for different interpolation radii

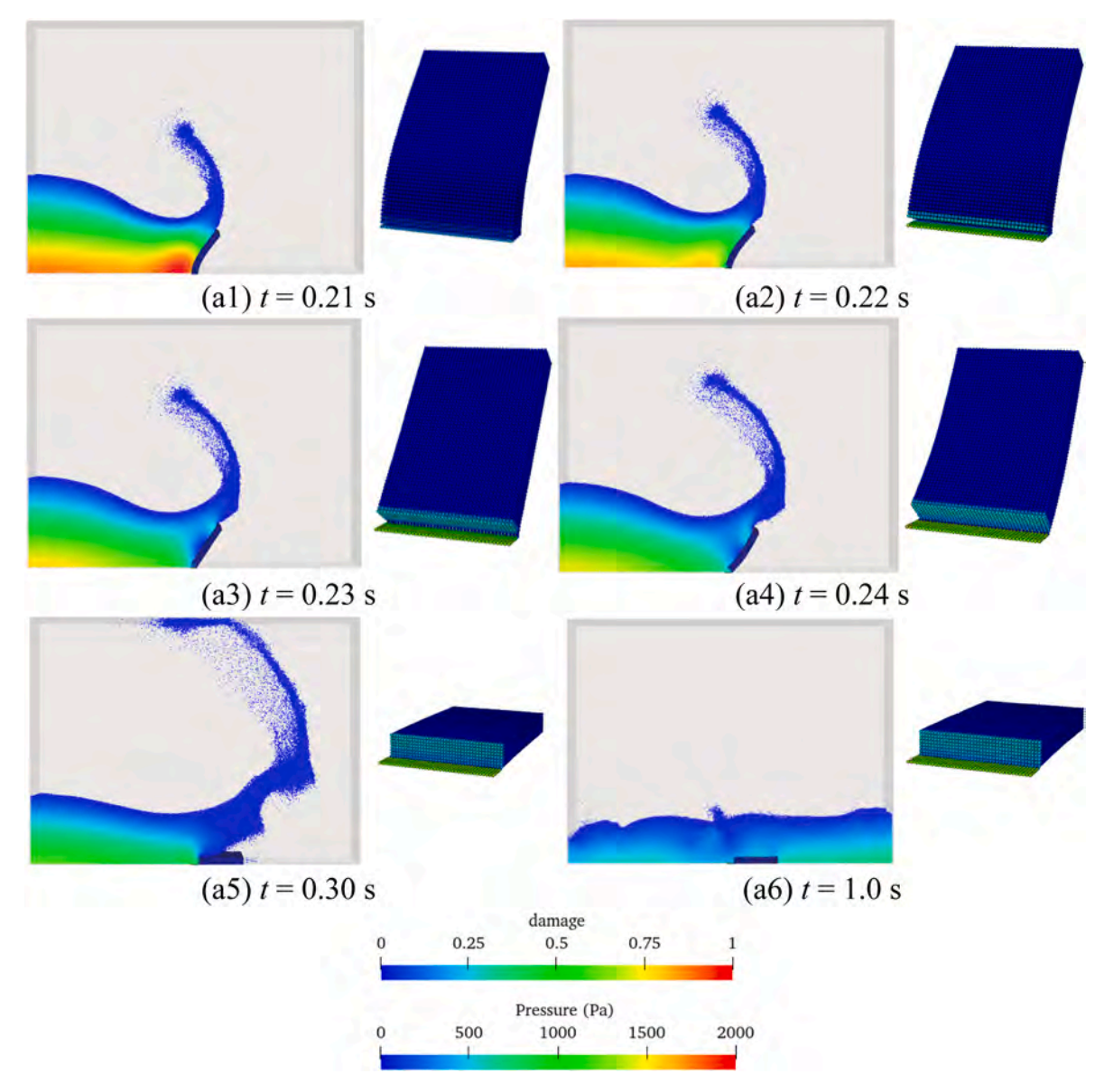
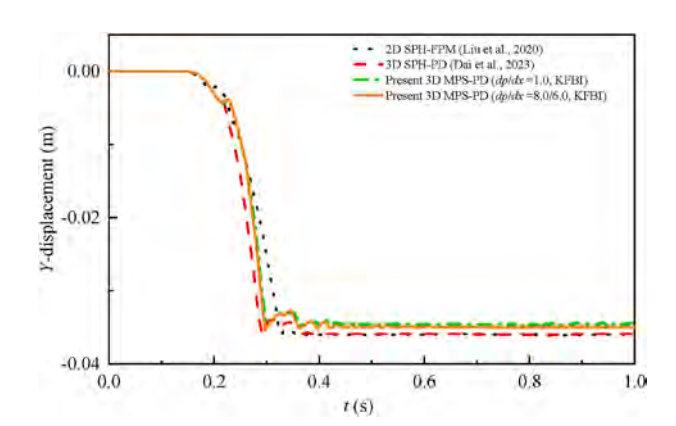


Fig. 37. Dam-break flow morphologies and structural damage produced by the present 3D MPS-PD - fracture of an elastic baffle induced by the dam-break flow.



**Fig. 38.** Comparison of vertical displacement time histories of the probe P2 among the numerical results obtained by 2D SPH-FPM (Liu et al., 2020), 3D SPH-PD (Dai et al., 2023), and the present 3D MPS-PD with different resolutions - fracture of an elastic baffle induced by the dam-break flow.

are relatively consistent and are in good agreement with the experimental results. Among them, the numerical simulation result of  $r_{ei}=3dp$  (where dp is the initial particle spacing of MPS) is slightly lower than those under other interpolation radii during the descending phase. This is because, as the influence radius increases, the pressure difference between adjacent regions exerted on the PD particles decreases. A convergence study is also conducted, as shown in Fig. 24. It can be observed that the numerical results with KFBI are almost identical to those with PtoP, which verifies the accuracy of KFBI. Besides, the numerical results with different resolutions show good agreement with each other, which indicates that the MPS-PD solver exhibits high convergence performance.

Fig. 25 shows the experimental snapshots and the corresponding numerical simulation results. At different times, both the flow morphology and the deformations of the elastic gate obtained by the MPS-PD solver are in good agreement with the experimental results. Moreover, both the flow field pressure distribution and structural stress distribution obtained from the simulation are very smooth and continuous, which further confirms the stability of the MPS-PD solver.

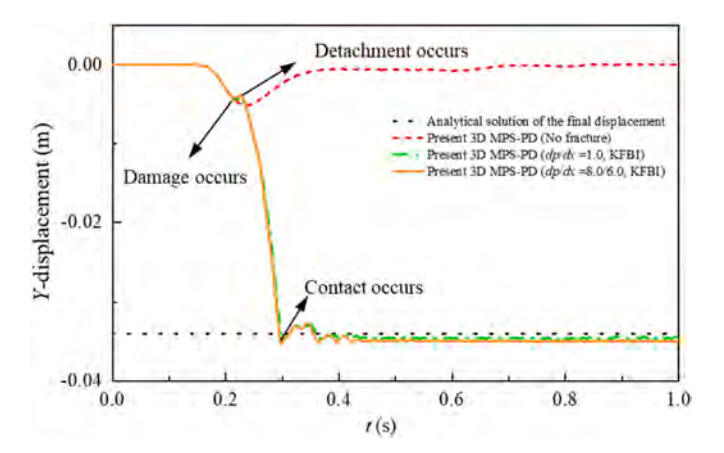


Fig. 39. Vertical displacement time histories of the probe P2 - fracture of an elastic baffle induced by the dam-break flow.

# 3.3.2. Deformation of an elastic plate induced by a hydrostatic water column

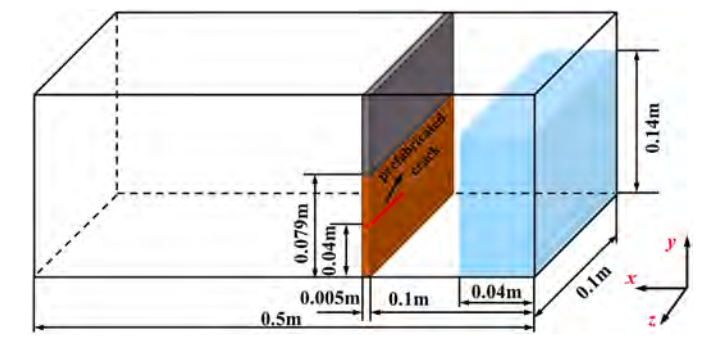
The accuracy and stability of the presented MPS-PD FSI solver are further evaluated through an FSI benchmark test of a hydrostatic water column on an elastic plate. This benchmark was first proposed by Fourey et al. (2017), and was extended for energy analysis (Khayyer et al., 2018) and three-dimensional scenarios (Khayyer et al., 2022b). Fig. 26 presents the schematic of the numerical model in the present study. A water column of 0.6 m in height and 0.4 m in length is placed on a both-end-clamped elastic plate with a thickness of 0.04 m. There is a deflection probe at the midpoint of the plate. Other parameters for simulation are listed in Table 7.

Fig. 27 presents the displacement time histories of the P probe. The analytical solution is obtained via the classical plate theory, and the detailed derivation process can be found in the literature (Khayyer et al., 2022b). Specifically, the maximum deflection at the midpoint of the elastic plate is  $1.14 \times 10^{-6} \, \mathrm{m}$ . It can be noticed that the numerical simulation results converge to the analytic solution as the PD resolution increases. When dp/dx=1.5, the numerical results obtained by MPS-PD are closest to the analytic solution, and the deflection at the midpoint of the plate is  $1.19 \times 10^{-6} \, \mathrm{m}$ . The pressure/stress fields at  $t=4.0 \, \mathrm{s}$  reproduced by the MPS-PD are shown in Fig. 28. It can be observed that the pressure/stress fields are very smooth, without the occurrence of non-physical oscillations.

The energy conservation of the entire FSI system is further evaluated. The formulation of each energy component can be expressed as:

$$E_T = E_T^S + E_T^F \tag{37}$$

where  $E_T^F$  denotes the total energy of the fluid field, which is composed of the kinetic energy  $E_K^F$  and potential energy  $E_P^F$  of the fluid, and is



**Fig. 40.** Schematic of the numerical model - fracture of a hanging plate with a prefabricated crack induced by the dam-break flow.

expressed as:

$$E_T^F = E_R^F + E_P^F \tag{38}$$

$$E_K^F = \sum_{i \in \mathcal{O}_P} \frac{1}{2} m_i^F |\mathbf{v}_i|^2, E_P^F = \sum_{i \in \mathcal{O}_P} m_i^F \mathbf{g} \cdot \mathbf{r}_i$$
(39)

Fig. 29 shows the time histories of normalized total energies. It can be observed that the curves under different PD resolutions maintain consistency. This is because the loss of total energy is mainly dominated by the gravitational potential energy of the fluid (Khayyer et al., 2018; Zhang et al., 2022a), while the MPS resolution is kept constant in this case study. It can be observed that the energy loss curve oscillates initially and eventually stabilizes at a constant value of -0.00177. In general, the MPS-PD solver exhibits good energy conservation performance.

# 3.3.3. Deformation of a hanging elastic plate induced by the dam-break flow

In this section, the MPS-PD solver is further validated by simulating the process of dam-break flow impacting a hanging elastic plate, which was experimentally investigated by Yilmaz et al. (2021). Fig. 30 presents the schematic of the numerical model. The length, width, and height of the numerical water tank are 1.58 m, 0.05 m, and 0.3 m, respectively. A water column with a length of 0.1 m, a width of 0.05 m, and a height of 0.2 m is located on the left side of the water tank. There is an elastic plate suspended from a rigid wall, 0.8 m away from the left wall of the numerical water tank, and the elastic plate's free end is 0.025 m above the tank's bottom. The elastic plate has a width of 0.05 m, a height of 0.125 m, and a thickness of 0.007 m. Other parameters for simulation are listed in Table 8.

Fig. 31 shows the flow morphologies and the deformations of the elastic plate at different times. The deformation of the elastic plate increases rapidly under the first impact of the dam-break flow, and then decreases quickly under the action of the restoring force. As the fluid accumulates on the left side of the elastic plate, its deformation increases again, and finally decreases gradually. It can be observed that both the shape of the dam-break flow and the deformation of the elastic plate simulated by MPS-PD are in good agreement with the experimental results. Furthermore, both the pressure distribution of the flow field and the stress distribution of the structure are very smooth and continuous without any non-physical oscillations.

Fig. 32 presents horizontal displacement time histories at different probes obtained by experiment (Yilmaz et al., 2021), 2D SPH-SPH (Meng et al., 2022), 2D SPH-PD (Liang et al., 2025a), 3D SPH-FEM (Chen et al., 2025), and the present 3D MPS-PD. It can be noticed that the displacement curves have two peaks, which is consistent with the phenomenon observed in Fig. 31. The displacement time histories obtained by the MPS-PD method are in good agreement with the experimental displacement time histories and those from other numerical methods in terms of peak values and overall trends.

Fig. 33 shows the MPS structural models and the PD structural

**Table 10**Parameters in the simulation - fracture of a hanging plate with a prefabricated crack induced by dam-break flow.

MPS parameters	Values	PD parameters	Values
Density (kg/m <sup>3</sup> )	1000	Density (kg/m <sup>3</sup> )	800
Initial particle spacing	$1.25 \times$	Initial particle spacing (m)	$1.0 \times$
(m)	$10^{-3}$		$10^{-3}$
Viscosity (Pa·s)	$8.9  imes 10^{-5}$	Young's modulus (Pa)	$9.7\times10^6$
Time step (s)	$2.5\times10^{-4}$	Poisson's ratio	0.17
-	-	Critical energy release rate	3.56
		$(J/m^2)$	
_	_	Critical bond stretch ratio $s_0$	0.01
_	-	Time step (s)	$5.0 \times$
			$10^{-6}$

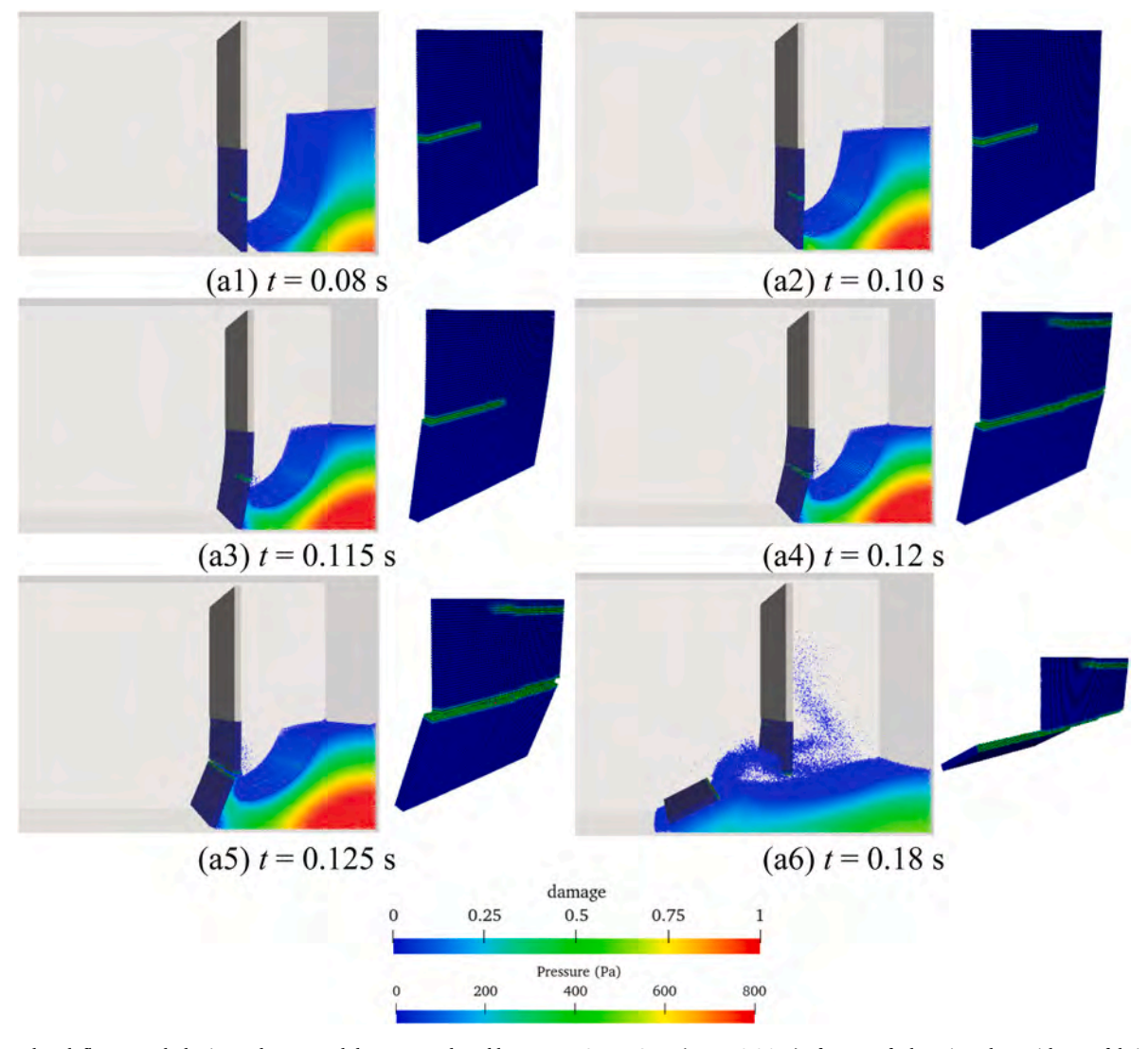


Fig. 41. Dam-break flow morphologies and structural damage produced by present 3D MPS-PD ( $L_{PC}=0.04~m$ ) - facture of a hanging plate with a prefabricated crack induced by the dam-break flow.

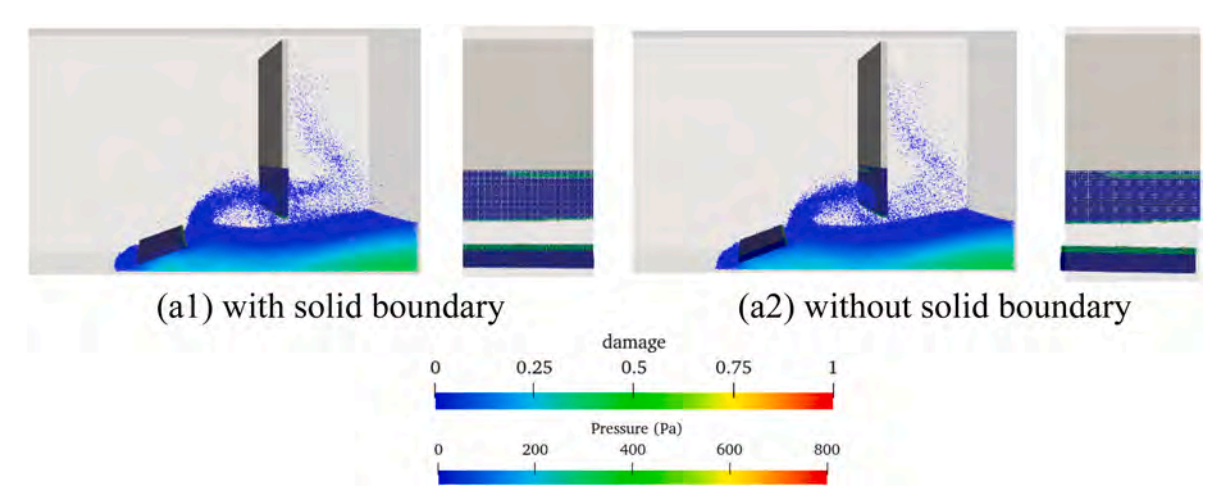
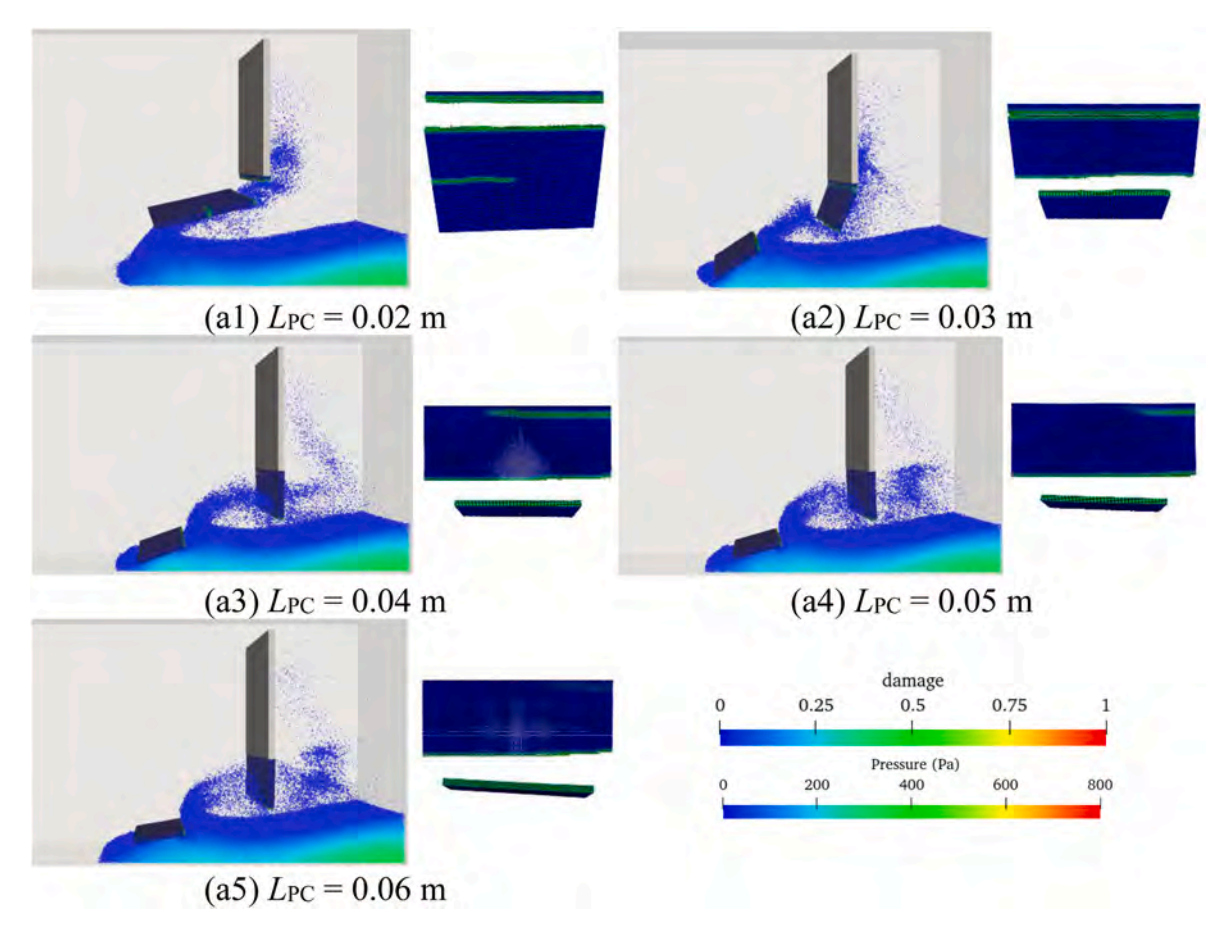
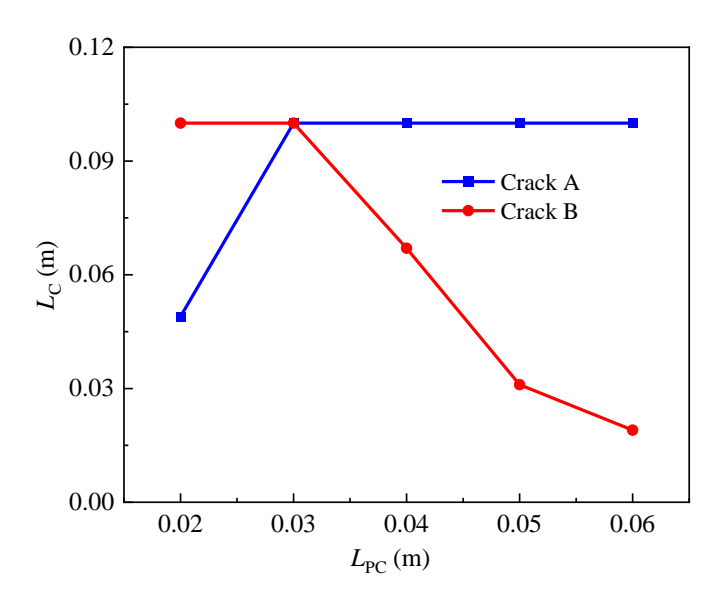


Fig. 42. Dam-break flow morphologies and structural damage obtained under different solid conditions at t = 0.2 s ( $L_{PC} = 0.04$  m) - fracture of a hanging plate with a prefabricated crack induced by the dam-break flow.



**Fig. 43.** Dam-break flow morphologies and structural damage obtained under different lengths of prefabricated cracks at t = 0.2 s - fracture of a hanging plate with apprefabricated crack induced by the dam-break flow.



**Fig. 44.** Final crack lengths versus different prefabricated crack lengths - fracture of a hanging plate with a prefabricated crack induced by the dambreak flow.

models with different resolutions at the same time. It can be observed that the deformations of the two models maintain consistency, and the pressure on the MPS models corresponds accurately to the stress in the PD models. KFBI exhibits high accuracy in fluid-structure interpolation within the MPS-PD solver.

# 3.3.4. Fracture of an elastic baffle induced by the dam-break flow

Fracture of an elastic baffle induced by dam-break flow is investigated in this section. The schematic of the numerical model is presented in Fig. 34. There is a water tank with a length of  $0.584\,\mathrm{m}$ , a width of  $0.06\,\mathrm{m}$ , and a height of  $0.438\,\mathrm{m}$ . A water column with a length of  $0.146\,\mathrm{m}$ , a width of  $0.06\,\mathrm{m}$ , and a height of  $0.292\,\mathrm{m}$  is on the left side of the water tank. There is an elastic baffle with a height of  $0.08\,\mathrm{m}$ , a width of  $0.04\,\mathrm{m}$ , and a thickness of  $0.0012\,\mathrm{m}$  located at the center of the bottom of the water tank. The bottom of the elastic baffle is rigidly fixed to the water tank, while its top is a free end. Other parameters are listed in Table 9.

Firstly, a numerical simulation is conducted on the case without elastic baffle fracture, and the value of the critical bond stretch ratio  $s_0$  is set to 1.0. The snapshots of the present numerical results are compared with those simulated by 2D SPH-FPM (Liu et al., 2020), as shown in Fig. 35. The simulation results demonstrate the key processes of dam-break flow–elastic baffle interaction, the deformation of the elastic baffle, the formation of an obvious tongue jet, and the subsequent jet impacting the rigid wall. The deformation of the elastic baffle and the shape of the free liquid surface obtained using 2D SPH-FPM and the present 3D MPS-PD are both in good agreement with each other. Furthermore, both the pressure distribution of the flow field and the stress distribution of the structure obtained by the proposed 3D MPS-PD solver are very smooth.

Horizontal displacement time histories of probe A among the numerical results obtained by 2D PFEM (Idelsohn et al., 2008), 2D SPH-FPM (Liu et al., 2020), 2D SPH-FEM (Long et al., 2016), 2D SFEM (Zhang et al., 2019), 3D SPH-PD (Dai et al., 2023), and the present 3D MPS-PD are presented in Fig. 36. Overall, the time histories obtained by different methods follow similar trends. Upon the contact of the dam-break flow with the baffle, negative displacement can be observed.

When  $t<0.6~\rm s$ , the rate of displacement increase, the magnitude of its peak value, and the rate of displacement decrease obtained by different methods are in good agreement. When  $t>0.6~\rm s$ , the back-and-forth deformation of the elastic baffle can also be well captured by different numerical methods.

Then, the fracture of the elastic baffle induced by dam-break flow is simulated by the present 3D MPS-PD, and the value of the critical bond stretch ratio  $s_0$  is set to 0.127. The dam-break flow morphologies and structural damage is presented in Fig. 37. Under the impact of the dambreak flow, the baffle deforms, and the stress at its ends increases gradually. When the deformation of the baffle reaches a certain extent, cracks start to appear at the fixed end of the baffle. With the continuous action of the dam-break flow, the cracks gradually expand, and finally the baffle detaches from the fixed end. It can be seen that the shape of the jet is obviously different from that in the case without baffle fracture. Although the baffle fractures rapidly and causes significant disturbance to the flow field, the pressure field remains relatively smooth, without non-physical oscillations, which further demonstrates the stability of the 3D MPS-PD method.

Fig. 38 plots vertical displacement time histories of the probe P2 obtained by numerical methods in the fracture case. Overall, the movement of the baffle produced by the present 3D MPS-PD agrees well with that by other methods. Furthermore, the numerical results under different resolutions are almost identical, which demonstrates that the KFBI technique can also maintain high interpolation accuracy in fracture problems. Displacement changes induced by fracture and contact are further presented in Fig. 39. When the baffle shows no damage, the displacements in the non-fracture case and those in the fracture case remain consistent. At t = 0.207 s, when the two curves separate, this indicates the occurrence of damage. At t = 0.301 s, the baffle exhibits reverse movement, indicating that it comes into contact with the wall. After multiple contacts with the bottom of the water tank, the displacement of the baffle stabilizes around a constant value. When t >0.45 s, the minor fluctuations in the displacement time histories are caused by fluid flow. The displacement of the P2 should be equal to the height of the P2 minus half of the baffle's thickness, which corresponds to the analytic solution. It can be observed that the maximum displacement obtained by the MPS-PD method is almost consistent with the analytic solution. The contact model adopted by the 3D MPS-PD solver is accurate and reliable.

# 3.3.5. Fracture of a hanging plate with a prefabricated crack induced by the dam-break flow

In this section, the proposed 3D MPS-PD solver is employed to investigate the interaction between dam-break flow and a vertically hanging plate with a prefabricated crack. The schematic of the numerical model is presented in Fig. 40. There is a water tank with a length of 0.5 m and a width of 0.1 m. A water column with a length of 0.04 m, a width of 0.05 m, and a height of 0.14 m is on the right side of the water tank. A hanging elastic plate with a width of 0.1 m, a height of 0.079 m, and a thickness of 0.005 m is located 0.1 m away from the right wall of the water tank. The top of the plate is the fixed end, and the bottom is the free end. There is a horizontal prefabricated crack on the plate, which is 0.04 m away from the bottom of the water tank. Other parameters can be found in Table 10.

Fig. 41 shows the dam-break flow morphologies and structural damage when the length of the prefabricated crack ( $L_{PC}$ ) is 0.04 m. It can be observed that at  $t \approx 0.115$  s, the fracture initiates first from the tip of the prefabricated crack, and this new crack formed by the fracture is referred to as Crack A. At  $t \approx 0.12$  s, a new Crack B initiates on the right side near the fixed end of the plate and propagates toward the left. At  $t \approx 0.12$  s, Crack A has traversed the entire plate, and a fragment detaches around the height of the prefabricated crack. Subsequently, some fluid climbs up along the fragment and forms a jet flow, which impacts the fracture surface of the remaining part of the plate at t = 0.18 s. It can be observed that due to the presence of the plate, the trajectory of the jet

flow changes, and no obvious particle penetration phenomenon is observed, which indicates that the fracture surface treatment method in the 3D MPS-PD method is reliable.

Fig. 42 presents dam-break flow morphologies and structural damage obtained under different boundary conditions. The DEM contact model is utilized in the case with solid boundary, while it is not employed in the case without solid boundary. It can be seen that in the case without a solid boundary, a part of the fragments is located outside the water tank, which is inconsistent with reality. Besides, in this case without solid boundary, the length of Crack B ( $L_{\rm C}=0.073~{\rm m}$ ) is significantly longer than that ( $L_{\rm C}=0.067{\rm m}$ ) in the case with a solid boundary. This is because without the constraint of the solid boundary, the plate can undergo greater torsional deformation. In conclusion, the DEM contact model adopted in this study is effective.

Fig. 43 and Fig. 44 compare the influence of the prefabricated crack lengths on structural damage. It can be seen that as the prefabricated crack length increases, the length of Crack A increases, while that of Crack B decreases. It is worth noting that when  $L_{\rm PC}=0.03$  m, both Crack A and Crack B eventually traverse the entire plate. However, the fragments only detach around the height of the prefabricated crack rather than from the ends of the plate. When  $L_{\rm PC}>0.03$  m, the fragments detach near the height of the prefabricated crack, whereas when  $L_{\rm PC}<0.03$  m, they detach near the ends of the plate.

In general, the 3D MPS-PD method is capable of reasonably predicting structural fracture behavior in violent FSI problems.

#### 4. Conclusions and prospects

In this paper, a 3D multi-resolution MPS-PD method is proposed to solve violent FSI problems involving structural deformation and fracture. Fluid pressure on the structural surface is transmitted from MPS wall particles to PD surface particles, while displacements and velocities are transmitted from PD structural particles to MPS structural particles. Besides, the KFBI technique is incorporated into the MPS-PD solver, enabling the flow field and structural field to be simulated at different resolutions.

Firstly, the accuracy of MPS solver is evaluated by simulating dambreak flow impacting a fixed square obstacle.

Secondly, the PD-based structural solver is validated by simulating several 3D benchmark tests, including an oscillating cantilever plate, a clamped-clamped beam under uniform load, the Kalthoff-Winkler impact test, and three-point bending of an ice beam. The displacement time histories of the structures at various resolutions exhibit good agreement with the analytic solutions, demonstrating good convergence performance of the developed PD solver. Furthermore, the stress fields exhibit spatial continuity and smoothness. In problems involving fracture, the cracks obtained from the simulations show good agreement with those from other numerical methods as well as experimental results; meanwhile, the energy dissipation caused by computational errors is relatively small, further confirming the accuracy of the developed PD solver.

Subsequently, the MPS-PD solver is utilized to investigate FSI problems, such as the flood discharge with an elastic plate, the hydrostatic water column on an elastic plate, the dam-break flow with a hanging elastic plate, and the dam-break flow with an elastic obstacle. The influence of the interpolation radius on computational results is evaluated. For different diameter ratios between fluid and structure particles, the simulated structural dynamic responses exhibit high consistency, confirming the accuracy of the interpolation method. Moreover, its results are in good agreement with the experimental results as well as those from other numerical methods. Furthermore, the FSI solver exhibits high energy conservation performance. Overall, the developed 3D MPS-PD solver is capable of accurately solving 3D FSI problems.

Finally, the MPS-PD solver is employed to investigate the dam-break flow impacting a hanging elastic plate with a prefabricated crack. Numerical results indicate that the length of prefabricated cracks exerts a significant influence on the extent of structural damage.

The PD model used in the present paper applies only to linear elastic materials; it therefore needs to be extended to plastic and composite materials for practical marine engineering applications, such as offshore platforms or ship hull fracture analysis (Pirzadeh et al., 2024, 2025). To further improve the accuracy of MPS-PD model, the adaptive refinement technique should be introduced to better simulate the interaction between fluid and fractures during the fracture process. Furthermore, integrating multi-GPU acceleration technology into the MPS-PD solver will enable tackling of more complex marine engineering problems—such as ship-water-ice interaction, a scenario that requires repeated establishment of PD neighbor particles and thus consumes considerable computational time.

#### CRediT authorship contribution statement

Fengze Xie: Writing – original draft, Visualization, Validation, Software, Investigation, Formal analysis, Data curation, Conceptualization. Jian Zhang: Visualization, Validation, Data curation. Yifan Li: Writing – review & editing, Visualization, Validation, Investigation, Data curation. Decheng Wan: Writing – review & editing, Supervision, Software, Resources, Project administration, Investigation, Funding acquisition, Data curation, Conceptualization. Moustafa Abdel-Maksoud: Writing – review & editing, Visualization, Validation, Investigation, Data curation.

#### Ethics approval and consent to participate

Not applicable.

#### Declaration of competing interest

The authors declare that they have no known competing financial interests or personal relationships that could have appeared to influence the work reported in this paper.

### Acknowledgments

This work was supported by the National Natural Science Foundation of China (52401334, 52131102), to which the authors are most grateful.

## Data availability

The data that support the findings of this study are available from the corresponding author upon reasonable request.

# References

- Antoci, C., Gallati, M., Sibilla, S., 2007. Numerical simulation of fluid-structure interaction by SPH. Comput. Struct. 85 (11–14), 879–890.
- Cao, C., Gu, C., Wang, C., Wang, C., Xu, P., Wang, H., 2024. A peridynamics-smoothed particle hydrodynamics coupling method for fluid-structure interaction. J. Mar. Sci. Eng. 12 (11).
- Chen, X., Cui, J., Li, J.Y., Shi, P.C., 2025. A hydroelastic fluid-structure interaction solver based on a coupled 3D SPH-FEM method. J. Fluid Struct. 137.
- Dai, Z., Xie, J., Jiang, M., 2023. A coupled peridynamics–smoothed particle hydrodynamics model for fracture analysis of fluid–structure interactions. Ocean Eng. 279.
- Dalla Barba, F., Zaccariotto, M., Galvanetto, U., Picano, F., 2022. 3D fluid-structure interaction with fracturing: a new method with applications. Comput. Methods Appl. Mech. Eng. 398.
- Di, S., 2015. Discrete element simulation of ice load on offshore platform and ship hull based on GPU parallel algorithm. In: Solid Mechanics. Dalian University of Technology, Dalian.
- Duan, G., Koshizuka, S., Yamaji, A., Chen, B., Li, X., Tamai, T., 2018. An accurate and stable multiphase moving particle semi-implicit method based on a corrective matrix for all particle interaction models. Int. J. Numer. Methods Eng. 115 (10), 1287–1314.
- Fimreite, S.B., Yu, Z., Amdahl, J., Greco, M., 2025. Numerical analysis of extreme water slamming damage and residual strength of ring-stiffened columns of a semi-submersible floating offshore wind turbine. Mar. Struct. 105.

- Fourey, G., Hermange, C., Le Touzé, D., Oger, G., 2017. An efficient FSI coupling strategy between Smoothed Particle Hydrodynamics and Finite Element methods. Comput. Phys. Commun. 217, 66–81.
- Gao, T., Fu, L., 2023. A new particle shifting technique for SPH methods based on Voronoi diagram and volume compensation. Comput. Methods Appl. Mech. Eng. 404
- Gotoh, H., Khayyer, A., Shimizu, Y., 2021. Entirely Lagrangian meshfree computational methods for hydroelastic fluid-structure interactions in ocean engineering—Reliability, adaptivity and generality. Appl. Ocean Res. 115.
- Gotoh, T., Khayyer, A., Gotoh, H., 2024. Enhanced schemes for resolution of the continuity equation in projection-based SPH. Eng. Anal. Bound. Elem. 166.
- Gotoh, T., Sakoda, D., Khayyer, A., Lee, C.H., Gil, A., Gotoh, H., Bonet, J., 2025. An enhanced total Lagrangian SPH for non-linear and finite strain elastic structural dynamics. Comput. Mech. 76 (1), 147–179.
- Huang, C., Wang, J., Zhao, W., Wan, D., 2024a. Numerical simulation of liquid sloshing in a spherical tank by MPS method. J. Hydrodyn. 36 (2), 232–240.
- Huang, C., Zhao, W., Wan, D., 2023. Numerical simulations of faraday waves in cylindrical and hexagonal tanks based on MPS method. J. Hydrodyn. 35 (2), 278–286
- Huang, D., Lu, G., Wang, C., Qiao, P., 2015. An extended peridynamic approach for deformation and fracture analysis. Eng. Fract. Mech. 141, 196–211.
- Huang, X., Zhu, B., Chen, Y., 2024b. A coupled peridynamics–smoothed particle hydrodynamics model for fluid–structure interaction with large deformation. Phys. Fluids 36 (11).
- Huang, X., Zhu, B., Chen, Y., 2025a. A coupled and parallel peridynamics–SPH modeling and simulation of buried explosion induced soil fragmentation and cratering. Comput. Geotech. 178.
- Huang, X., Zhu, B., Chen, Y., 2025b. A rate-dependent peridynamic–SPH coupling model for damage and failure analysis of concrete dam structures subjected to underwater explosions. Int. J. Impact Eng. 200, 105270.
- Huang, X.T., Sun, P.N., Lyu, H.G., Zhang, A.M., 2022. Numerical investigations on bionic propulsion problems using the multi-resolution Delta-plus SPH model. Eur. J. Mech. B Fluid 95, 106–121.
- Hwang, S.C., Khayyer, A., Gotoh, H., Park, J.C., 2014. Development of a fully Lagrangian MPS-based coupled method for simulation of fluid-structure interaction problems. J. Fluid Struct. 50, 497–511.
- Idelsohn, S.R., Marti, J., Limache, A., Oñate, E., 2008. Unified lagrangian formulation for elastic solids and incompressible fluids: application to fluid-structure interaction problems via the PFEM. Comput. Methods Appl. Mech. Eng. 197 (19–20), 1762–1776.
- Iwamoto, T., Nakase, H., Nishiura, D., Sakaguchi, H., Miyamoto, J., Tsurugasaki, K., Kiyono, J., 2019. Application of SPH-DEM coupled method to failure simulation of a caisson type composite breakwater during a tsunami. Soil Dynam. Earthq. Eng. 127.
- Ji, S., Wang, A., Su, J., Yue, Q., 2011. Experimental studies on elastic modulus and flexural strength of sea ice in the Bohai Sea. J. Cold Reg. Eng. 25 (4).
- Jing, C., Wang, Y., Ju, L., Wang, Q., Xue, Y., Li, J., 2024. A coupled smoothed particle hydrodynamics-peridynamics model for two-dimensional hydroelastic water entry. Phys. Fluids 36 (8).
- Kalthoff, J.F., 2000. Modes of dynamic shear failure in solids. Int. J. Fract. 101, 1–31.
  Khayyer, A., Gotoh, H., 2011. Enhancement of stability and accuracy of the moving particle semi-implicit method. J. Comput. Phys. 230 (8), 3093–3118.
- Khayyer, A., Gotoh, H., 2012. A 3D higher order Laplacian model for enhancement and stabilization of pressure calculation in 3D MPS-based simulations. Appl. Ocean Res. 37, 120–126.
- Khayyer, A., Gotoh, H., Falahaty, H., Shimizu, Y., 2018. An enhanced ISPH–SPH coupled method for simulation of incompressible fluid–elastic structure interactions. Comput. Phys. Commun. 232, 139–164.
- Khayyer, A., Gotoh, H., Shimizu, Y., 2022a. On systematic development of FSI solvers in the context of particle methods. J. Hydrodyn. 34 (3), 395–407.
- Khayyer, A., Gotoh, H., Shimizu, Y., Gotoh, T., 2024. An improved Riemann SPH-Hamiltonian SPH coupled solver for hydroelastic fluid-structure interactions. Eng. Anal. Bound. Elem. 158, 332–355.
- Khayyer, A., Shimizu, Y., Gotoh, H., Hattori, S., 2021a. Multi-resolution ISPH-SPH for accurate and efficient simulation of hydroelastic fluid-structure interactions in ocean engineering. Ocean Eng. 226.
- Khayyer, A., Shimizu, Y., Gotoh, H., Hattori, S., 2022b. A 3D SPH-based entirely Lagrangian meshfree hydroelastic FSI solver for anisotropic composite structures. Appl. Math. Model. 112, 560–613.
- Khayyer, A., Shimizu, Y., Gotoh, H., Nagashima, K., 2021b. A coupled incompressible SPH-Hamiltonian SPH solver for hydroelastic FSI corresponding to composite structures. Appl. Math. Model. 94, 242–271.
- Khayyer, A., Shimizu, Y., Gotoh, T., Gotoh, H., 2023. Enhanced resolution of the continuity equation in explicit weakly compressible SPH simulations of incompressible free-surface fluid flows. Appl. Math. Model. 116, 84–121.
- Khayyer, A., Tsuruta, N., Shimizu, Y., Gotoh, H., 2019. Multi-resolution MPS for incompressible fluid-elastic structure interactions in ocean engineering. Appl. Ocean Res. 82, 397–414.
- Kleefsman, K.M.T., Fekken, G., Veldman, A.E.P., Iwanowski, B., Buchner, B., 2005. A volume-of-fluid based simulation method for wave impact problems. J. Comput. Phys. 206 (1), 363–393.
- Koshizuka, S., Oka, Y., 1996. Moving-particle semi-implicit method for fragmentation of incompressible fluid. Nucl. Sci. Eng. 123 (3), 421–434.
- Li, S., Lu, H., Huang, X., Yang, J., Sun, P., 2022. Numerical simulation of crack propagation and coalescence in marine cast iron materials using ordinary state-based peridynamics. Ocean Eng. 266.

- Li, Z., Leduc, J., Nunez-Ramirez, J., Combescure, A., Marongiu, J.-C., 2015. A non-intrusive partitioned approach to couple smoothed particle hydrodynamics and finite element methods for transient fluid-structure interaction problems with large interface motion. Comput. Mech. 55 (4), 697–718.
- Liang, G.Q., Sun, P.N., Lyu, H.G., Zhang, G.Y., 2025a. A coupled  $\delta$ +-SPH-NOSB-PD method: towards fluid-structure interaction problems involving violent free-surface flows and isotropic structural linear elastic deformations and failures. Appl. Math. Model. 145.
- Liang, G.Q., Sun, P.N., Lyu, H.G., Zhang, G.Y., 2025b. Establishment of a 3D numerical ice tank and its applications to ice-water-structure interactions based on a multiresolution SPH-PD coupled method. Comput. Struct. 316.
- Liu, F., Yu, Y., Wang, Q., Luo, Y., 2020. A coupled smoothed particle hydrodynamic and finite particle method: an efficient approach for fluid-solid interaction problems involving free-surface flow and solid failure. Eng. Anal. Bound. Elem. 118, 143–155.
- Liu, X., He, S., Huang, W., Wang, X., 2025. A stabilized LSMPS for three-dimensional complex free-surface flow with moving wall. Comput. Methods Appl. Mech. Eng. 441
- Liu, X., Morita, K., Zhang, S., 2019. A stable moving particle semi-implicit method with renormalized Laplacian model improved for incompressible free-surface flows. Comput. Methods Appl. Mech. Eng. 356, 199–219.
- Long, T., Hu, D., Yang, G., Wan, D., 2016. A particle-element contact algorithm incorporated into the coupling methods of FEM-ISPH and FEM-WCSPH for FSI problems. Ocean Eng. 123, 154–163.
- Lyu, H.G., Sun, P.N., Huang, X.T., Peng, Y.X., Liu, N.N., Zhang, X., Xu, Y., Zhang, A.M., 2023. SPHydro: promoting smoothed particle hydrodynamics method toward extensive applications in ocean engineering. Phys. Fluids 35 (1).
- Ma, C., Iijima, K., Oka, M., 2020. Nonlinear waves in a floating thin elastic plate, predicted by a coupled SPH and FEM simulation and by an analytical solution. Ocean Eng. 204.
- Madenci, E., Oterkus, E., 2014. Peridynamic Theory and Its Applications. Springer. Meng, Z.F., Zhang, A.M., Yan, J.L., Wang, P.P., Khayyer, A., 2022. A hydroelastic fluid-structure interaction solver based on the Riemann-SPH method. Comput. Methods Appl. Mech. Eng. 390.
- Ni, B.Y., Pan, Y.T., Yuan, G.Y., Xue, Y.Z., 2021. An experimental study on the interaction between a bubble and an ice floe with a hole. Cold Reg. Sci. Technol. 187.
- Pirzadeh, A., Dalla Barba, F., Bobaru, F., Sanavia, L., Zaccariotto, M., Galvanetto, U., 2024. Elastoplastic peridynamic formulation for materials with isotropic and kinematic hardening. Eng. Comput. 40 (4), 2063–2082.
- Pirzadeh, A., Dalla Barba, F., Sanavia, L., Zaccariotto, M., Galvanetto, U., 2025. State-based peridynamic modeling of fracture in \$\text{textrm{J}\_2\$\$-elastoplastic materials. Eng. Comput. 41 (4), 2559–2570.
- Rahimi, M.N., Kolukisa, D.C., Yildiz, M., Ozbulut, M., Kefal, A., 2022. A generalized hybrid smoothed particle hydrodynamics-peridynamics algorithm with a novel Lagrangian mapping for solution and failure analysis of fluid-structure interaction problems. Comput. Methods Appl. Mech. Eng. 389.
- Rahimi, M.N., Moutsanidis, G., 2023. An SPH-based FSI framework for phase-field modeling of brittle fracture under extreme hydrodynamic events. Eng. Comput. 39 (4) 2365–2399
- Ren, D., Park, J.C., 2023. Particle-based numerical simulation of continuous ice-breaking process by an icebreaker. Ocean Eng. 270.
- Shimizu, Y., Khayyer, A., Gotoh, H., 2022. An SPH-based fully-Lagrangian meshfree implicit FSI solver with high-order discretization terms. Eng. Anal. Bound. Elem. 137, 160–181.
- Silling, S.A., 2000. Reformulation of elasticity theory for discontinuities and long-range forces. J. Mech. Phys. Solid. 48, 175–209.
- Singh, V., Peng, C., Islam, M.R.I., 2025. Three-dimensional SPH modeling of brittle fracture under hydrodynamic loading. Comput. Fluid 301.
- Sun, P., Ming, F., Zhang, A., 2015. Numerical simulation of interactions between free surface and rigid body using a robust SPH method. Ocean Eng. 98, 32–49.
- Sun, P.N., Colagrossi, A., Le Touzé, D., Zhang, A.M., 2019. Extension of the δ-Plus-SPH model for simulating vortex-induced-vibration problems. J. Fluid Struct. 90, 19–42.
- Sun, P.N., Colagrossi, A., Marrone, S., Antuono, M., Zhang, A.M., 2018. Multi-resolution Delta-plus-SPH with tensile instability control: towards high Reynolds number flows. Comput. Phys. Commun. 224, 63–80.
- Sun, P.N., Le Touzé, D., Oger, G., Zhang, A.M., 2021. An accurate FSI-SPH modeling of challenging fluid-structure interaction problems in two and three dimensions. Ocean Eng. 221.
- Tanaka, M., Masunaga, T., 2010. Stabilization and smoothing of pressure in MPS method by Quasi-Compressibility. J. Comput. Phys. 229 (11), 4279–4290.

- Wang, Z., Zhang, C., Haidn, O.J., Hu, X., 2023. An eulerian SPH method with WENO reconstruction for compressible and incompressible flows. J. Hydrodyn. 35 (2), 210–221.
- Wu, D., Tang, X., Zhang, S., Hu, X., 2024. Unified non-hourglass formulation for total lagrangian SPH solid dynamics. Comput. Mech. 75 (3), 1081–1113.
- Wu, F., 2024. Consistent ordinary state-based peridynamics and its computational methods for fracture. In: Computational Mechanics. Dalian University of Technology, Dalian.
- Xie, F., Pan, G., Zhao, W., Wan, D., 2025. Unresolved MPS-DEM coupling method for three-dimensional liquid-solid dam-break flows impacting on rigid structures. Ocean Eng. 323.
- Xie, F., Zhao, W., Wan, D., 2020. CFD simulations of three-dimensional violent sloshing flows in tanks based on MPS and GPU. J. Hydrodyn. 32 (4), 672–683.
- Xie, F., Zhao, W., Wan, D., 2021a. MPS-DEM coupling method for interaction between fluid and thin elastic structures. Ocean Eng. 236.
- Xie, F., Zhao, W., Wan, D., 2021b. Numerical simulations of liquid-solid flows with free surface by coupling IMPS and DEM. Appl. Ocean Res. 114.
- Xie, F., Zhao, W., Wan, D., 2022. Overview of moving particle semi-implicit techniques for hydrodynamic problems in Ocean engineering. J. Mar. Sci. Appl. 21 (3), 1–22.
- Xiong, W., Wang, X., Wang, C., Galvanetto, U., Zaccariotto, M., 2025. Numerical study of an ice body impacting a cantilever plate based on an OSBPD-FEM hybrid method. Ocean Eng. 319.
- Xue, Y., Lu, X., Wang, Q., Bai, X., Li, Z., 2018. Simulation of three-point bending test of ice based on peridynamic. Harbin Gongcheng Daxue Xuebao/J. Harbin Eng. Univers. 39 (4), 607–613.
- Yang, F., Gu, X., Xia, X., Zhang, Q., 2022. A peridynamics-immersed boundary-lattice Boltzmann method for fluid-structure interaction analysis. Ocean Eng. 264.
- Yao, X., Chen, D., Wu, L., Huang, D., 2023. A multi-resolution DFPM-PD model for efficient solution of FSI problems with structural deformation and failure. Eng. Anal. Bound. Elem. 157, 424–440.
- Yao, X., Huang, D., 2022. Coupled PD-SPH modeling for fluid-structure interaction problems with large deformation and fracturing. Comput. Struct. 270.
- Yilmaz, A., Kocaman, S., Demirci, M., 2021. Numerical modeling of the dam-break wave impact on elastic sluice gate: a new benchmark case for hydroelasticity problems. Ocean Eng. 231.
- Zhan, Y., Luo, M., Khayyer, A., 2025a. DualSPHysics+: an enhanced DualSPHysics with improvements in accuracy, energy conservation and resolution of the continuity equation. Comput. Phys. Commun. 306.
- Zhan, Y., Luo, M., Khayyer, A., 2025b. An enhanced numerical wave tank for wavestructure interaction based on DualSPHysics+. Ocean Eng. 340.
- Zhan, Y., Luo, M., Khayyer, A., 2025c. An enhanced SPH-based hydroelastic FSI solver with structural dynamic hourglass control. J. Fluid Struct. 135.
- Zhang, G., Zha, R., Wan, D., 2022a. MPS-FEM coupled method for 3D dam-break flows with elastic gate structures. Eur. J. Mech. B Fluid 94, 171–189.
- Zhang, G., Zhao, W., Wan, D., 2022b. Moving Particle Semi-implicit method coupled with Finite Element Method for hydroelastic responses of floating structures in waves. Eur. J. Mech. B Fluid 95, 63–82.
- Zhang, H., Qiao, P., 2018. A state-based peridynamic model for quantitative fracture analysis. Int. J. Fract. 211 (1–2), 217–235.
- Zhang, H., Qiao, P., 2020. A two-dimensional ordinary state-based peridynamic model for elastic and fracture analysis. Eng. Fract. Mech. 232.
- Zhang, S., Wu, D., Lourenço, S.D.N., Hu, X., 2025. A generalized non-hourglass updated Lagrangian formulation for SPH solid dynamics. Comput. Methods Appl. Mech. Eng. 440
- Zhang, Y., Wan, D., 2017. Numerical study of interactions between waves and free rolling body by IMPS method. Comput. Fluid 155, 124–133.
- Zhang, Y., Wan, D., 2018. MPS-FEM coupled method for sloshing flows in an elastic tank. Ocean Eng. 152, 416–427.
- Zhang, Y., Wan, D., Hino, T., 2014. Comparative study of MPS method and level-set method for sloshing flows. J. Hydrodyn. 26 (4), 577–585.
- Zhang, Z.L., Long, T., Chang, J.Z., Liu, M.B., 2019. A smoothed particle element method (SPEM) for modeling fluid–structure interaction problems with large fluid deformations. Comput. Methods Appl. Mech. Eng. 356, 261–293.
- Zhao, W., Yang, X., Wan, D., 2024. Numerical analysis of coupled sloshing and motion of a cylindrical FPSO in regular waves. J. Hydrodyn. 36 (3), 457–465.
- Zhuang, Y., Zhou, F., Zhou, W., Wan, D., 2023. Numerical investigations of focused wave interact with a moving cylinder. J. Hydrodyn. 35 (4), 724–735.